

¹ **Copyright**
² **by**
³ **Ryan Patrick Hannigan**
⁴ **2023**

5 The Dissertation Committee for Ryan Patrick Hannigan certifies that
6 this is the approved version of the following dissertation:

7 **Stranger Things at the LHC**

Committee:

Christina Markert, Supervisor

Peter Onyisi

Aaron Zimmerman

Chandrajit Bajaj

9

Stranger Things at the LHC

10

by

11

Ryan Patrick Hannigan, Ph.D.

12

Dissertation

13

Presented to the Faculty of the Graduate School of

14

The University of Texas at Austin

15

in Partial Fulfillment

16

of the Requirements

17

for the degree of

18

Doctor of Philosophy

19

The University of Texas at Austin

20

May, 2023

To Jaynee.

Chapter One: Introduction

23 The initial section of this chapter will mostly serve as a historical overview of the
24 field of particle physics, leading to the development of the **Standard Model**: the
25 theory that describes all of the fundamental¹ particles and the way in which they
26 interact with each other. An emphasis will be made on the discovery of quarks and
27 gluons, as the research presented in this thesis is centered around these particles.
28 The second section will more thoroughly introduce the Standard Model and its three
29 distinct sectors, with the goal to provide a high-level mathematical overview of the
30 theory.

31 The third section of this chapter will delve into the details of Quantum Chromo-
32 Dynamics (QCD), which is the component of the Standard Model that describes the
33 interactions between **quarks** and **gluons**, the constituent particles of the more famil-
34 iar protons and neutrons. As many theoretical calculations are difficult to perform
35 in QCD, the use of computationally-intensive numerical techniques is often required
36 to make precise predictions. One such prediction is a phase transition from nuclear
37 matter at everyday energies—in which the quarks and gluons are confined within
38 protons and neutrons—into a novel state of matter at extreme temperatures or den-
39 sities, known as the **Quark-Gluon Plasma** (QGP). Section 1.4 will detail the QGP
40 and many of its interesting properties predicted by QCD, with an emphasis on the
41 production of strange quarks within the plasma.

42 The final two sections of this chapter will discuss how high-energy particle col-
43 lisions can be used to study the QGP, using both expensive particle accelerators
44 (Section ??) and simulation techniques (Section 1.7).

¹As of the year 2023, but reading this chapter will hopefully illustrate why this may be subject to change in the (likely very distant) future.

45 1.1 What is fundamental?

46 The answer to the question

47 What are the fundamental building blocks of our universe?

48 has changed drastically over the course of human history. The idea that all matter
49 is composed of smaller, uncuttable pieces has been around since 5th century BCE
50 when Greek philosophers Democritus and Leucippus first introduced the concept of
51 an atom [1]. While this idea was mostly motivated by philosophical reasoning, it was
52 later adopted by the English scientist John Dalton in the 19th century to explain the
53 results of his chemical experiments, where he found that chemical elements always
54 combined with each other by discrete units of mass [2]. As scientists discovered more
55 and more of these elements, the number of “fundamental” building blocks grew as
56 well. By the late 1800s, over 70 unique chemical elements had been discovered, though
57 they would often be grouped together due to similar chemical properties using what
58 chemist Dimitri Mendeleev dubbed the *periodic table of elements* [3]. An example of
59 the periodic table from the time of Mendeleev can be seen in Figure 1.1. While this
60 grouping was useful for chemists, it also served as a hint to physicists that perhaps
61 these elements were not actually fundamental, but rather composed of even smaller
62 pieces.

		Ti = 50	Zr = 90	? = 180
		V = 51	Nb = 94	Ta = 182
		Cr = 52	Mo = 96	W = 186
		Mn = 55	Rh = 104,4	Pt = 197,4
		Fe = 56	Ru = 104,4	Ir = 198
		Ni = Co = 59	Pd = 106,6	Os = 199
H = 1		Cu = 63,4	Ag = 108	Hg = 200
	Be = 9,4	Zn = 65,2	Cd = 112	
	B = 11	Al = 27,4	? = 68	Uu = 197?
	C = 12	Si = 28	? = 70	Sn = 118
	N = 14	P = 31	As = 75	Sb = 122
	O = 16	S = 32	Se = 79,4	Te = 128?
	F = 19	Cl = 35,5	Br = 80	J = 127
Li = 7	Na = 23	K = 39	Rb = 85,4	Cs = 133
		Ca = 40	Sr = 87,6	Ba = 137
		? = 45	Ce = 92	Tl = 204
		?Er = 56	La = 94	Pb = 207
		?Yt = 60	Di = 95	
		?In = 75,6	Th = 118?	

Figure 1.1: Dimitri Mendeleev’s periodic table of elements from the late 1800s, taken from [4]. The elements are grouped by similar chemical properties, and the gaps in the table are where Mendeleev predicted that new elements would be discovered.

63 Scientists' understanding of the building blocks of matter changed again around
64 the turn of the 20th century, with physicists J.J. Thomson, Ernest Rutherford, and
65 James Chadwick determining that the supposedly indivisible atom was composed
66 of even smaller subatomic particles, eventually named electrons, protons, and neu-
67 trons [5]–[7]. Thus the number of fundamental blocks of matter had decreased sub-
68 stantially from nearly 100 to just three. However, this number would need to be
69 updated again only months later, as the fundamental anti-particle of the electron—
70 known as the positron—was discovered in 1932 by Carl Anderson [8]. In the next two
71 decades, the number of known fundamental particles would skyrocket. In 1947, the
72 muon was discovered [9], followed by the discovery of a laundry list of particles [10]–
73 [12] that participate in the same interaction that holds the positively charged protons
74 together in the nucleus of an atom—the so-called **strong nuclear force**. These “fun-
75 damental” particles were collectively called **hadrons**, which were further separated
76 into lighter and heavier categories, dubbed **mesons** and **baryons**, respectively [13].
77 By the late 1960s, the number of known hadrons had grown to well over 100 [14],
78 even more than the number of “fundamental” chemical elements that were known to
79 exist in the 1800s.

80 In the same way that Mendeleev tried to group the elements by their similar
81 chemical properties, physicists attempted to group the hadrons together based on
82 their known subatomic properties. The first successful attempt at such a grouping
83 was the **Eightfold Way**, which was independently proposed by Murray Gell-Mann
84 and Yuval Ne’eman in 1961 [15], [16]. This grouping was found by examining the
85 following properties of the hadrons:

- 86 1. **Isotopic spin:** a quantum number introduced by Werner Heisenberg in 1932
87 to try to explain the apparent symmetries between the proton and neutron
88 with respect to the strong nuclear force [17] (i.e. although the proton and
89 neutron have different electric charges, the strong interaction does not seem to
90 distinguish between the two)
- 91 2. **Strangeness:** another quantum number introduced by Gell-Mann and Nishi-
92 jima in 1953 to explain why some hadrons decayed much more slowly than
93 expected, and such particles appeared to be created in pairs [18]. In other
94 words, the strong interaction responsible for the creation of these particles ap-
95 peared to conserve this quantum number, but the weak interaction responsible

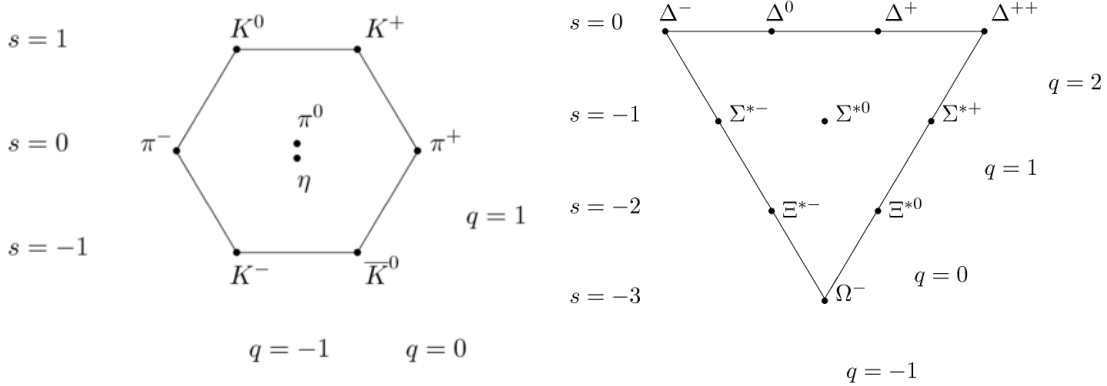


Figure 1.2: The “Eightfold Way” diagrams of the $J = 1/2$ mesons (left) and $J = 3/2$ baryons (right) plotted against strangeness and electric charge. Understanding the underlying symmetry group that gives rise to such patterns³ ultimately led to the development of the quark model. While the original patterns were found using isotopic spin and hypercharge, it is trivial to convert between the two using the Gell-Mann-Nishijima formula [19], [20].

96 for the slower decay of these particles did not. Strangeness² will be discussed
 97 in more detail in Section 1.3.2.5.

98 Plotting the baryons and mesons in a two-dimensional space based on these two
 99 properties revealed striking patterns, as shown in Figure 1.2. Similar to Mendeleev,
 100 GellMann also left a blank space⁴ where he believed a new particle—the Ω^- —would
 101 be discovered. The patterns in these diagrams hinted at an underlying symmetry
 102 governing the strong nuclear force, and ultimately led to the invention of the very
 103 first quark model by Gell-Mann and Zweig in 1964 [21]. This model proposed that
 104 all of the hadrons were actually composed of even smaller particles, which Gell-Mann
 105 dubbed “quarks”. The quark model was able to explain the patterns seen in Figure 1.2
 106 by introducing three different types of fermionic quarks—up, down and strange—along
 107 with their corresponding anti-quarks. Baryons would then be composed of three such

²The “strangeness” being referred to in this section was introduced a few years before the very first quark model, but it now has the modern interpretation which is directly related to the number of strange and anti-strange quarks within a hadron.

³Namely $SU(3)$, but this is a history lesson. Also the path from $SU(3)$ to patterns of this type is long and arduous, involving a thorough understanding of representation theory.

⁴The original paper on the Eightfold Way does not contain any of these diagrams, but there are discussions about the properties of particles that should exist if the theory were correct, but had not been observed [15].

108 quarks, whereas mesons would be composed of quark and anti-quark pairs. If the
109 quark model were correct, the number of fundamental building blocks of matter would
110 again decrease from over 100 to just 14: electrons, muons, electron neutrinos, muon
111 neutrinos, up quarks, down quarks, strange quarks, and all of their corresponding
112 anti-particles.

113 Initially, many physicists believed that the quarks from this model were just a
114 mathematical abstraction [22]. This possibility did not stop Sheldon Glashow and
115 James Bjorken from extending the quark model less than a year after its inception by
116 introducing a fourth quark: the charm [23]. This new quark was primarily introduced
117 to equalize the number of leptons (four at the time: electron, muon, and their re-
118 spective neutrinos) with the number of quarks. The theory was mostly aesthetic [24]
119 in that the charm quark was not explicitly required by any known mechanisms. It
120 was only after the Glashow-Iliopoulos-Maiani (GIM) mechanism was introduced in
121 1970 [25] that the existence of the charm quark became necessary. This mechanism
122 helped explain why neutral kaons decayed into two muons at a much lower rate than
123 expected, but it required the existence of a quark with the same charge as the up
124 quark but with a much larger mass.

125 The notion that protons and neutrons were fundamental particles was also being
126 challenged on the experimental side. The deep inelastic scattering experiments at the
127 Stanford Linear Accelerator Center (SLAC) performed by Kendall, Friedman, and
128 Taylor in 1968 [26]–[28] revealed unexpected⁵ behavior when probing the structure
129 of the proton: it appeared to be composed of point-like particles. These experiments
130 were performed by firing electrons at stationary protons and measuring the energy
131 distributions of the scattered electrons at different scattering angles. An example
132 of such a distribution for electrons with initial energies of 10 GeV scattered at 6
133 degrees can be seen in Figure 1.3. The large spike on the left side of the distribution
134 corresponds to the elastic scattering of the electron off the proton, which was well
135 understood at the time [29]. The “bumps” observed at lower values of the scattered
136 electron energy were also well understood [30], and they correspond to the “shallow”
137 inelastic scattering of the electron off the proton, where the proton gets excited into a
138 so-called *resonance* state (like the Δ baryon). However, the “background” underneath
139 the bumps and the apparent continuum of events at even lower values of the scattered

⁵Depending on who you asked at the time, both the three and four quark models were not universally accepted.

140 electron energy corresponded to a host of unknown particles being produced. This
 141 host of particles appeared to grow with increasing scattering angle and decreasing
 142 scattered electron energy, which ultimately led to the conclusion that the proton was
 143 composed of point-like particles that were being “knocked out” of the proton by the
 144 incoming electron [26], [31].

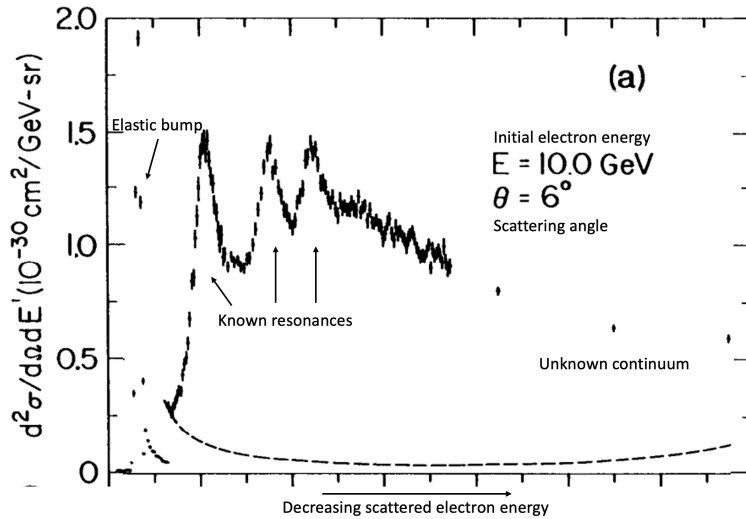


Figure 1.3: The energy distribution of electrons scattered off of protons at an initial electron energy of 10 GeV and a scattering angle of 6 degrees. The large spike on the left side of the distribution corresponds to the elastic scattering of the electron off the proton, and the “bumps” correspond to the inelastic scattering of the electron off the proton. The “background” underneath the bumps and the apparent continuum of events at even lower values of the scattered electron energy correspond to a mess of unknown particles being produced. The behavior of this continuum with respect to the scattering angle and the scattered electron energy ultimately led to the conclusion that the proton was not fundamental.

145 While many physicists were perfectly happy to interpret these point-like parti-
 146 cles as the very same quarks from the aforementioned quark model(s), they received
 147 the much more noncommittal name **partons** after Richard Feynman’s parton model
 148 of hadrons [32]. The association of these partons with quarks was not universally
 149 accepted⁶ until the discovery of the J/ψ meson in 1974 [33]. In the meantime, the
 150 theoretical description of the strong nuclear force was closing in on its final form.

⁶No acceptance of any model is a step function, but the discovery of J/ψ seems to be a turning point in literature.

151 The formulation of Quantum ChromoDynamics (QCD) in the early 1970s by Gell-
152 Mann, Fritzsch, and Leutwyler [34] resolved many of the issues that were present in
153 the initial quark models⁷. QCD introduced the concept of color charge, which all of
154 the quarks would carry. The mediating bosons of the strong interaction—known as
155 **gluons**—were also introduced, carrying color charge as well.

156 While QCD gave a solid mathematical description of the strong interaction, it
157 wasn’t until the discovery of **asymptotic freedom** [35], [36] by Gross, Wilczek, and
158 Politzer in 1973 that the theory became experimentally testable. Asymptotic freedom
159 refers to the property that the strong interaction becomes weaker at higher energies,
160 allowing for QCD calculations to be performed using perturbative techniques. This
161 discovery allowed theorists to use QCD to make predictions of the results of very
162 high energy particle collision experiments. The first QCD prediction to be experimen-
163 tally verified came from the Positron-Electron Tandem Ring Accelerator (PETRA)
164 in 1979 [37], which experimentally confirmed the existence of gluons [38]. With ex-
165 perimental verification of QCD, it became clear that the association of partons with
166 quarks was indeed incorrect: they are both quarks *and* gluons.

167 In addition to the theory of QCD, the theory of electroweak interactions was
168 also being developed during the 1960s by Glashow, Weinberg, and Salam [39], [40].
169 With this new theory came the prediction of four⁸ new bosons: the Higgs boson, the
170 charged W^\pm bosons, and the neutral Z^0 boson. With the combined theories of the
171 electroweak and strong interaction, the **Standard Model** of particle physics—which
172 describes the now 61⁹ fundamental particles and how they interact—was complete.

173 1.2 The Standard Model

174 The Standard Model of particle physics is a **quantum field theory** (QFT) that
175 describes the interactions between all¹⁰ of the fundamental particles. QFTs describe
176 the dynamics of a quantum system in terms of fields, which are functions of space and

⁷For example, the wavefunction of the Δ^{++} baryon under the first quark model was not anti-symmetric, which is a requirement for fermions.

⁸The Higgs mechanism (which predicts the existence of the Higgs boson) came before electroweak unification [41], but it was a requirement for the theory.

⁹There are many ways to count fundamental particles, but this particular number is obtained by: 6 leptons ($\times 2$ for anti-leptons), 6 quarks ($\times 3$ for each color, $\times 2$ for anti-quarks), 1 gluon ($\times 8$ for color), 1 photon, the W and Z bosons, and the Higgs boson.

¹⁰Ignoring potential gravitons [42] or dark matter candidates [43]

177 time. The fields are the fundamental objects of QFT, and their excitations correspond
178 to the particles that are observed in nature. The Standard Model fields can be broken
179 down into three sectors, which will be discussed in the following sections.

180 **1.2.1 The gauge sector**

181 The gauge sector of the Standard Model corresponds to the spin-one bosons that
182 mediate the strong and electroweak interactions. In a general sense, this sector corre-
183 sponds to the mediating particles for three of the four fundamental forces: the strong
184 nuclear force, the weak nuclear force, and the electromagnetic force. The fourth
185 fundamental force—gravity—is not included in the Standard Model, as it is not yet
186 understood from a quantum perspective [44].

187 The symmetry group of the gauge sector is given by

$$\text{SU}(3)_c \times [\text{SU}(2)_L \times \text{U}(1)_Y]. \quad (1.1)$$

188 $\text{SU}(3)_c$ is the symmetry group of the strong interaction, which is described by the QFT
189 known as Quantum ChromoDynamics (QCD). The subscript c stands for “color”,
190 indicating that the gauge fields in QCD (gluons) only couple to colored objects. QCD
191 will be discussed in more detail in Section 1.3. The symmetry group of the electroweak
192 interaction is $\text{SU}(2)_L \times \text{U}(1)_Y$, where the subscript L stands for “left-handed” and the
193 subscript Y stands for “weak hypercharge”. Again, these subscripts indicate the types
194 of objects to which the corresponding gauge fields couple. For example, the gauge
195 fields of $\text{SU}(2)_L$ only couple to left-handed objects, and the gauge fields of $\text{U}(1)_Y$
196 only couple to weakly hypercharged objects. Initially, there are four massless gauge
197 fields in the electroweak theory ¹¹. After the spontaneous symmetry breaking of the
198 Higgs mechanism [41], these fields mix to give rise to three massive gauge fields and
199 one massless gauge field. The three massive gauge fields correspond to the familiar
200 W^\pm and Z^0 bosons, which are the mediating bosons of the weak interaction. The
201 massless gauge field corresponds to the photon, which mediates the electromagnetic
202 interaction.

¹¹Three corresponding to the generators of $\text{SU}(2)$, one corresponding to the generator of $\text{U}(1)$.

203 **1.2.2 The scalar sector**

204 The scalar sector of the Standard Model is quite lonely, and only corresponds to
205 one spin-zero field: the Higgs [41]. As mentioned in the previous section, the Higgs
206 mechanism that corresponds to this field is responsible for the acquisition of mass
207 by the W^\pm and Z^0 bosons. The Higgs field also couples to all of the fermions in the
208 Standard Model, but the mass acquisition procedure is *slightly* different¹² from the
209 massive bosons. The associated Higgs boson was discovered by the A Toroidal LHC
210 Apparatus (ATLAS) and Compact Muon Solenoid (CMS) collaborations in 2012 [45],
211 [46], and was the last major piece of the Standard Model to be experimentally verified.

212 **1.2.3 The fermionic sector**

213 The fermionic sector contains all of the spin one-half particles (quarks and leptons) in
214 the Standard Model. It is often convenient to group these particles into three genera-
215 tions, where each generation is identical except for the masses of the particles. It is
216 even *more* convenient to group the fermions within each family into multiplets, where
217 the members of the multiplet are related to each other by transformations within the
218 gauge group of the Standard Model (Equation 1.1). In other words, the fermions
219 within a particular multiplet can only be transformed to fermions within the same
220 multiplet. A table of the fermions in the Standard Model and their corresponding
221 multiplets can be seen in Table 1.1. The indices L and R correspond to the chirality
222 of the fields, and the indices r , g , and b represent the color charge of the fields. The
223 color charges are only non-zero for the quarks, making them the only fermions that
224 couple to the gauge fields of the strong interaction (gluons).

225 **1.3 Quantum chromodynamics**

226 Quantum chromodynamics (QCD) is the component of the Standard Model that
227 describes the strong interaction between quarks and gluons, the fundamental particles
228 that make up most of the matter in the universe. In this theory, the fermionic quarks
229 have “color charge”, which can either be red, green or blue for quarks, or anti-red,
230 anti-green, or anti-blue for anti-quarks. The gluons, which are the mediating bosons

¹²It’s still spontaneous symmetry breaking, but within the Yukawa part of the electroweak La-
grangian.

Table 1.1: The fermions of the Standard Model for each generation and their corresponding multiplets. The Standard Model does not allow for fermions to leave their respective multiplets.

Gen.	Left-handed quarks	Right-handed up quarks	Right-handed down quarks	Left- handed leptons	Right- handed leptons
1 st gen.	$\begin{pmatrix} u_L^r & u_L^g & u_L^b \\ d_L^r & d_L^g & d_L^b \end{pmatrix}$	$(u_R^r \ u_R^g \ u_R^b)$	$(d_R^r \ d_R^g \ d_R^b)$	$\begin{pmatrix} \nu_{eL} \\ e_L \end{pmatrix}$	(e_R)
2 nd gen.	$\begin{pmatrix} c_L^r & c_L^g & c_L^b \\ s_L^r & s_L^g & s_L^b \end{pmatrix}$	$(c_R^r \ c_R^g \ c_R^b)$	$(s_R^r \ s_R^g \ s_R^b)$	$\begin{pmatrix} \nu_{\mu L} \\ \mu_L \end{pmatrix}$	(μ_R)
3 rd gen.	$\begin{pmatrix} t_L^r & t_L^g & t_L^b \\ b_L^r & b_L^g & b_L^b \end{pmatrix}$	$(t_R^r \ t_R^g \ t_R^b)$	$(b_R^r \ b_R^g \ b_R^b)$	$\begin{pmatrix} \nu_{\tau L} \\ \tau_L \end{pmatrix}$	(τ_R)

231 of the strong interaction, also carry color charge, but in the form of a superposition of
 232 both color and anti-color. This section will delve into the details of QCD, emphasizing
 233 the properties of the strong interaction that make it so challenging to study.

234 1.3.1 The QCD Lagrangian

The dynamics of the Standard Model fields and how they interact are completely encoded within the Lagrangian of the theory, which can be used to calculate experimental observables like cross-sections and decay rates. However, the Lagrangian of the Standard Model is fairly long [47], and often not particularly insightful when trying to study a specific aspect of the theory. As such, when studying QCD, it is often useful to throw away the electroweak gauge fields, leptons, and scalars to look at only the QCD Lagrangian [48],

$$\mathcal{L}_{QCD} = -\frac{1}{4}F_{\mu\nu}^A F^{A\mu\nu} + i\bar{q}\gamma^\mu \left(\partial_\mu + ig_s \frac{1}{2}\lambda^A \mathcal{A}_\mu^A \right) q - \bar{q}_R \mathcal{M} q_L - \bar{q}_L \mathcal{M}^\dagger q_R - \theta\omega,$$

235 where all repeated indices are summed over.

236 The gluons are described by the vector gauge field \mathcal{A}_μ^A , with index A representing
 237 one of the eight color labels. These eight components belong to the color group
 238 $SU_c(3)$, which is the gauge group of QCD. The corresponding coupling constant is
 239 g_s , and the field strength tensor $F_{\mu\nu}^A$ is given by

$$F_{\mu\nu}^A = \partial_\mu \mathcal{A}_\nu^A - \partial_\nu \mathcal{A}_\mu^A + g_s f^{ABC} \mathcal{A}_\mu^B \mathcal{A}_\nu^C, \quad (1.2)$$

240 where f^{ABC} are the structure constants [49] of $SU_c(3)$. Note that while this field
 241 strength tensor shares the same letters as the electromagnetic field strength tensor
 242 $F_{\mu\nu}$, the additional term $g_s f^{ABC} \mathcal{A}_\mu^B \mathcal{A}_\nu^C$ in Equation 1.2 separates QCD and QED in a
 243 very fundamental way: the gluons are allowed to self-interact. This self-interaction is
 244 a direct result of the non-vanishing structure constants of $SU_c(3)$ ¹³, and is responsible
 245 for the challenging nature of QCD calculations.

246 The quarks are represented by the field q , where the color, flavor and spin indices
 247 have been suppressed. In reality, the quark field q has:

- 248 • six flavor indices $\{u, d, s, c, b, t\}$,
- 249 • four spin indices $\{0, 1, 2, 3\}$, and
- 250 • three color indices $\{r, g, b\}$,

251 where all of these indices are being implicitly summed over in \mathcal{L}_{QCD} . Luckily, all of
 252 the matrices $(\mathcal{A}_\mu^A, \lambda^A, \mathcal{M}, \gamma^\mu)$ act on separate sets of indices¹⁴. For example, the γ^μ s
 253 only operate on the spin indices, whereas both the gluon fields \mathcal{A}_μ^A and Gell-Mann
 254 matrices [15] λ^A operate on the color indices. These Gell-Mann matrices are the
 255 generators of $SU_c(3)$ and satisfy the commutation relation

$$[\lambda^A, \lambda^B] = 2i f^{ABC} \lambda^C. \quad (1.3)$$

256 The chiral quark fields q_L and q_R are defined as $\frac{1}{2}(1-\gamma_5)q$ and $\frac{1}{2}(1+\gamma_5)q$, respectively.
 257 The mass matrix \mathcal{M} operates on the flavor indices, and its form depends on the choice
 258 of basis for the quark fields [48]. It is often convenient to choose a basis where the
 259 mass matrix is diagonal, which can be done by independent rotations of q_L and q_R in
 260 $SU(6)$. Doing so gives the more familiar term

$$-\bar{q}_R \mathcal{M} q_L - \bar{q}_L \mathcal{M}^\dagger q_R = - \sum_{f=1}^6 \bar{q}_f m_f q_f, \quad (1.4)$$

261 where m_f is the mass of the quark with flavor f , and q_f is the flavor component of
 262 the quark field. Note that this term completely violates the $SU(2) \times U(1)$ electroweak
 263 symmetry, indicating that the given \mathcal{L}_{QCD} is determined *after* the spontaneous sym-
 264 metry breaking described in the previous section.

¹³Structure constants of Abelian gauge groups like $U(1)$ are trivially zero.

¹⁴Really the components of the field corresponding to those indices.

265 These quark masses are also subject to **renormalization** [50], which is a process
266 that removes the infinities that arise from the self-interaction of the quarks and gluons.
267 The renormalization process results in the running of the quark masses with respect
268 to the energy scale μ of the interaction¹⁵. More simply, the quark masses are inversely
269 dependent on this energy scale: at large μ , the quark masses are small, and at lower
270 μ , the quark masses are large. At the energy scale $\mu \approx 2$ GeV (close to the mass of the
271 proton), the masses of the up, down, and strange quarks—collectively referred to as
272 the light-flavor quarks—are approximately $2.2 \text{ MeV}/c^2$, $4.7 \text{ MeV}/c^2$, and $96 \text{ MeV}/c^2$,
273 respectively [52]. The heavy-flavor charm, bottom, and top quarks have masses of
274 approximately $1.28 \text{ GeV}/c^2$, $4.18 \text{ GeV}/c^2$, and $173 \text{ GeV}/c^2$, respectively¹⁶.

275 The final term, known as the θ -term [53], is something of a mystery. It is a
276 scalar term that violates CP symmetry [54], and is often set to zero as there is no
277 experimental evidence for its existence. However, it is not clear why this term is zero,
278 as there is no symmetry that explicitly forbids it. This is known as the **strong CP**
279 **problem**, and is one of the biggest open questions in particle physics [55].

280 **1.3.1.1 Brief aside: Why eight gluons?**

281 The gluon field \mathcal{A}^A transforms under the adjoint representation of SU(3), which
282 is a representation of SU(3) on the vector space of its Lie algebra $\mathfrak{su}(3)$. As $\mathfrak{su}(3)$
283 has eight basis elements (for instance, the Gell-Mann matrices λ^A from above), the
284 adjoint representation of SU(3) is eight-dimensional. Thus the gluon field has eight
285 independent components, or, equivalently, there are eight gluons. In principle, QCD
286 could have been built on top of a U(3) gauge group, which would give rise to nine
287 gluons (as the dimension of U(n) is n^2). However, the singlet state in U(3) would be
288 required to be non-interacting; if it were, color neutral baryons would interact with
289 each other via the strong interaction at a much longer range [56]. Such interactions
290 have not been observed [57]. As there is no physical difference between U(3) with a
291 non-interacting singlet and SU(3), the simpler gauge group was chosen.

¹⁵They also depend on the *choice* of renormalization scheme, with the most commonly implemented one being minimal subtraction or MS [51].

¹⁶At the energy scale governed by their respective masses (i.e. $\mu = m_Q$). [52]

292 **1.3.2 Properties of QCD**

293 **1.3.2.1 Confinement**

294 One of the unique properties of QCD is the phenomenon of **confinement**, which is
295 the observation that quarks and gluons are never seen in isolation. Instead, they are
296 *confined* inside of the color neutral bound states known as hadrons. This property
297 is mostly understood in terms of the coupling constant g_s . The renormalization [58]
298 of QCD gives rise to a g_s that varies with energy scale or distance. As the distance
299 between two quarks increases, so too does g_s . At some point, the coupling becomes so
300 strong that the energy required to separate the quarks is enough to create a quark-
301 anti-quark pair from the vacuum. Thus any attempts to separate a quark from a
302 hadron will always result in the creation of a new hadron, making it impossible to
303 observe single quarks in isolation.

304 The large coupling constant in this low energy regime makes it impossible to
305 describe this phenomenon using perturbative techniques, so the exact mechanism of
306 confinement is still not fully understood. However, it is often described using the
307 phenomenological Lund string model [59]. In this model, the field lines of two quarks
308 are pulled together due to the self-interaction of the gluons. This creates a string-like
309 structure between the two quarks, with a potential given by

$$V(r) \approx -\frac{4}{3} \frac{\alpha_s}{r} + \kappa r, \quad (1.5)$$

310 where r is the distance between the two quarks, $\alpha_s = \frac{g_s^2}{4\pi}$ and κ is the string tension.
311 This can be contrasted with the potential between two electrically charged particles,
312 where the field lines are not pulled together and become less dense as the distance
313 between the two particles increases. As such, the potential decreases with increasing
314 distance, opposite to that of the Lund model. A schematic of these differences can
315 be seen in Figure 1.4.

316 **1.3.2.2 Asymptotic freedom**

317 Just as the coupling constant becomes large at low energies and large distances, it
318 also becomes small at high energies and small distances. This property is known
319 as **asymptotic freedom**: at high enough energies, the quarks and gluons can be
320 thought of as “free”, and their interactions can be modeled using perturbative QCD

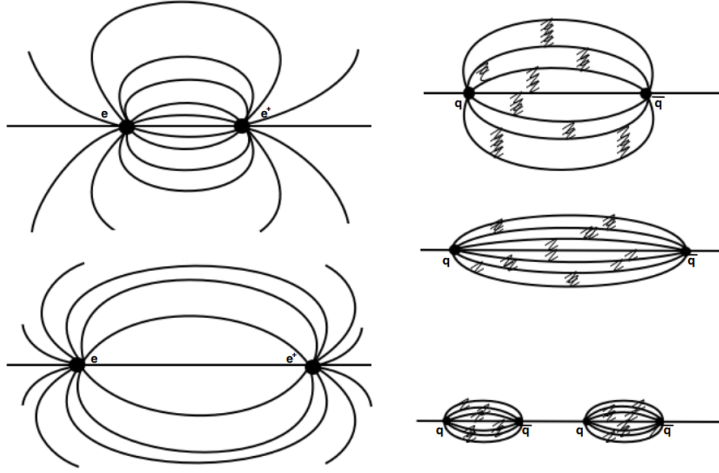


Figure 1.4: A schematic of the field lines between two electrically charged particles (left) and two quarks (right). The field lines between the quarks are pulled together due to the self-interaction of the gluons, whereas the electric field lines are not.

321 (pQCD). As discussed in Section 1.1, the discovery of asymptotic freedom in QCD was
 322 what allowed for the accurate predictions of the results of high energy particle collision
 323 experiments like SLAC [60] and PETRA [37]. The results of such experiments have
 324 also been used to calculate the value of the coupling constant itself at different energy
 325 scales, as shown in Figure 1.5. The value of α_s at the Z^0 mass is also given in the
 326 figure, which is the most accurate measurement of α_s to date [52].

327 1.3.2.3 Chiral symmetry breaking

328 The mass term in the QCD Lagrangian,

$$-\bar{q}_R \mathcal{M} q_L - \bar{q}_L \mathcal{M}^\dagger q_R, \quad (1.6)$$

329 explicitly breaks **chiral symmetry**: swapping the left-handed and right-handed com-
 330 ponents of the quark fields does not leave the Lagrangian invariant. The breaking of
 331 chiral symmetry due to the non-zero quark masses is referred to as **explicit** chiral
 332 symmetry breaking.

333 However, even in the limit of massless quarks, chiral symmetry is broken by the
 334 QCD vacuum. This is known as **spontaneous** chiral symmetry breaking, and due

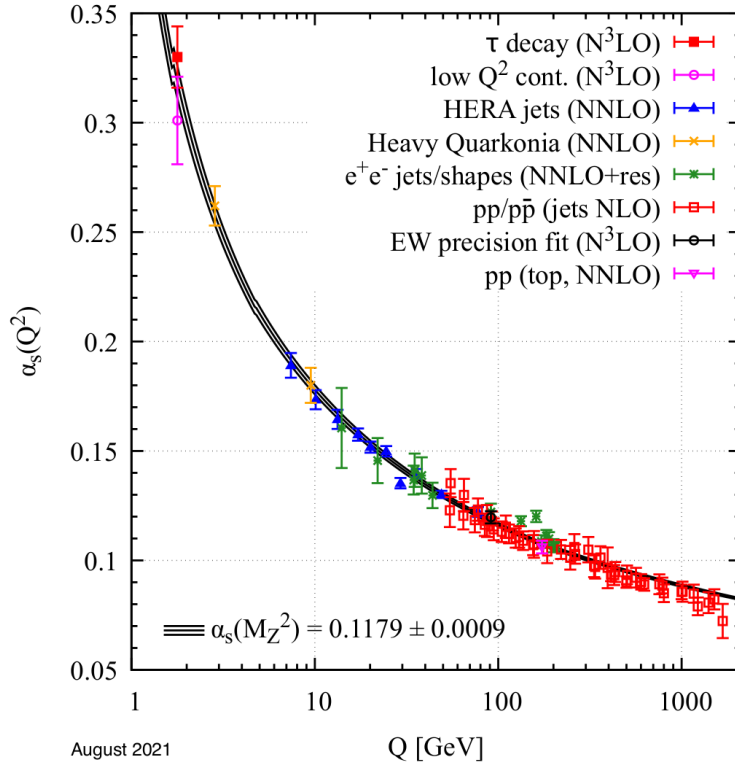


Figure 1.5: The value of the strong coupling constant α_s as a function of momentum transfer Q , which represents the energy scale of the interaction.

335 to the non-zero vacuum expectation value of the quark condensate [61]

$$\langle \bar{q}q \rangle = \langle \bar{q}_L q_R + \bar{q}_R q_L \rangle \neq 0. \quad (1.7)$$

336 This non-zero value is a direct result of the confinement of QCD **TongGaugeTheory**
 337 (Section 1.3.2.1), and implies that the ground state of the theory is filled with quark-
 338 anti-quark pairs. The spontaneous breaking of chiral symmetry in QCD gives rise
 339 to eight massless Nambu-Goldstone bosons **NambuGoldstone**, which are the pseudo-
 340 scalar mesons $\pi^{\pm,0}$, $K^{\pm,0}$, η , and η' . These mesons then acquire a small mass due
 341 to the aforementioned explicit chiral symmetry breaking from the quark masses.

342 1.3.2.4 Jets

343 During high energy particle collisions (between two protons, for example), the con-
 344 stituent partons of the protons will sometimes scatter off each other in a way that con-

verts most of their initial longitudinal momentum (along the collision axis) into transverse momentum (in the plane perpendicular to the collision axis). Such a scattering is often referred to as a **hard scattering**. Because the momentum transfer is large, the cross-section of the parton-parton scattering is calculable using pQCD. Furthermore, branching processes of the high momentum partons—like gluon radiation—can also be calculated perturbatively. Eventually, however, the partons will lose enough energy such that their behavior can no longer be described using perturbative techniques.

Luckily, the aforementioned Lund model is well-equipped to deal with lower energy partons. Under the Lund model, as these colored partons move away from each other, the force between them increases until there is enough energy to produce a quark-anti-quark pair (as discussed in Section 1.3.2.1). This process—known as string fragmentation—continues until the partons are no longer energetic enough to move away from each other, at which point they hadronize into a large number of color neutral bound states. These particles are roughly collimated in the direction(s) of the initial hard scattering, forming sprays of hadrons known as **jets**. A diagram depicting the formation of a jet from an initial hard scattering of partons can be seen in Figure 1.6.

1.3.2.5 Flavor conservation

One interesting feature of the interactions in QCD is that all **flavor** quantum numbers are conserved. Specifically, the number of quarks minus the number of anti-quarks of each flavor is a conserved quantity in every strong interaction¹⁷. In this thesis, the most important flavor quantum number is **strangeness**, which is defined as

$$S = -(n_s - n_{\bar{s}}), \quad (1.8)$$

where n_s is the number of strange quarks and $n_{\bar{s}}$ is the number of strange anti-quarks. The “minus” sign in front of the expression indicates that the strangeness of a strange quark is negative (-1), and the strangeness of a strange anti-quark is positive ($+1$).

¹⁷Conservation of the “historical” flavor quantum number *isospin* (from Section 1.1), which is $+\frac{1}{2}$ for up quarks and $-\frac{1}{2}$ for down quarks, is equivalent to the conservation of $n_{u,d} - n_{\bar{u},\bar{d}}$ when baryon number is considered. Baryon number is an absolutely conserved quantum number in the Standard Model [52], and (anti-)quarks have baryon number $(-)\frac{1}{3}$.

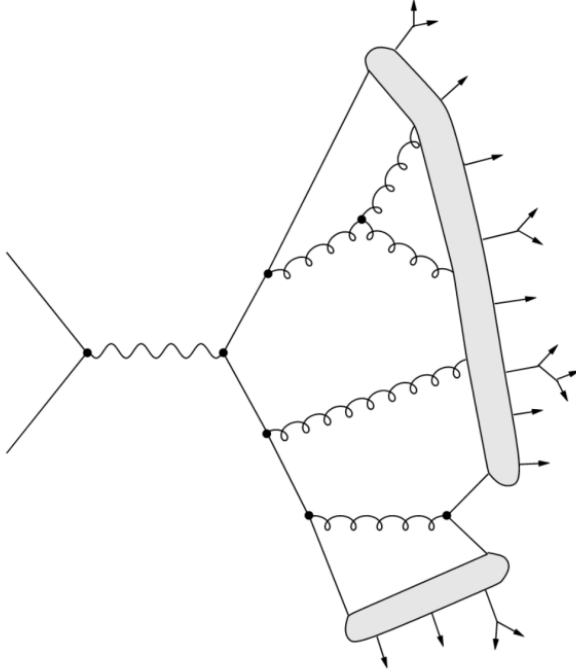


Figure 1.6: A diagram depicting the formation of a jet within the Lund model from an initial hard scattering of partons, adapted from [62]. The vertices represent perturbative QCD processes, the shaded regions represent string fragmentation/hadronization, and the outgoing arrows represent the resulting hadrons (which may decay further).

371 This convention is chosen¹⁸ to make the signs of these “flavor charges” consistent
 372 with the signs of the electric charges of these quarks, which are $-\frac{1}{3}$ for the strange
 373 quark and $+\frac{1}{3}$ for the strange anti-quark. Strangeness conservation has an interesting
 374 consequence for particle collisions between atomic nuclei: as the total strangeness of
 375 these nuclei (protons and neutrons) is zero, the number of strange and anti-strange
 376 quarks produced from the strong interaction during these collisions must be equal.
 377 In other words, the production of strange quarks in these collisions must come in the
 378 form of strange quark-anti-quark ($s\bar{s}$) pairs.

¹⁸Really this is a historical convention that stems from the fact that “strangeness” was introduced as a concept before the existence of any quark models, as mentioned in Section 1.1.

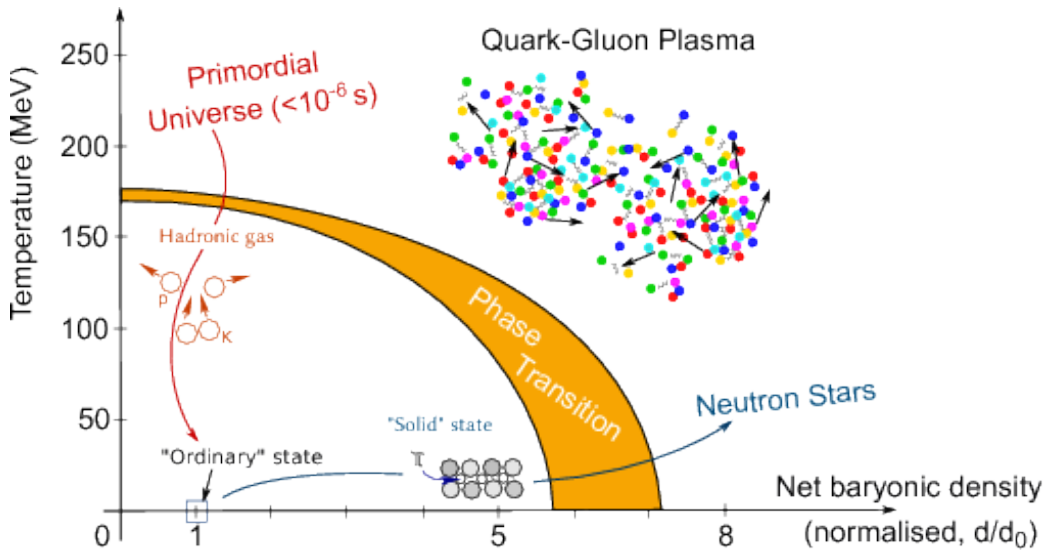


Figure 1.7: A phase diagram of the QGP, taken from [65]. The axes are temperature and baryon density, and the orange band represents the phase transition from normal hadronic matter to the QGP.

379 1.4 The Quark-Gluon Plasma

380 One of the consequences of the asymptotic freedom of QCD is the prediction of
 381 a new state of matter at extreme temperatures and densities: the **quark-gluon**
 382 **plasma** (QGP) [63], [64]. In this plasma, the quarks and gluons are not confined
 383 inside hadrons, and instead behave as quasi-free particles. This is analogous to an
 384 electromagnetic plasma, where electrons and protons are dissociated from their atoms.
 385 A phase diagram of this plasma can be seen in Figure 1.7. This diagram has two
 386 axes: temperature and baryon density. Increasing *either* of these quantities beyond
 387 a certain threshold will cause a phase transition from normal hadronic matter to the
 388 QGP. Similarities can be drawn between this phase diagram and that of a snowball:
 389 heating *or* squeezing a snowball will cause it to melt into a liquid¹⁹.

390 Numerical simulations of QCD on a lattice **LatticeQCD1**, **LatticeQCD2** (known
 391 as lattice QCD or lQCD) have shown that at zero baryon density, the transition from
 392 hadronic matter to the QGP occurs as a smooth crossover **LatticeQCD Crossover**
 393 with a critical temperature $T_C \approx 160$ MeV or 10^{12} K, 10,000 times hotter than the cen-

¹⁹Be careful: if you continue to heat up the snowball enough, or squeeze hard enough, it will undergo another phase transition into the QGP.

394 ter of the sun. LQCD has also been used to predict the existence of a critical endpoint
395 in the QGP phase diagram at a non-zero baryon density **LatticeQCD.CriticalPoint**,
396 beyond which the transition from hadronic matter to the QGP is no longer a smooth
397 crossover, but a first-order phase transition. However, due to the complex action
398 problem **ComplexActionProblem**, lQCD simulations at non-zero baryon density
399 are not yet possible²⁰. Thus the exact location of this critical endpoint is still un-
400 known, and is the subject of much experimental and theoretical research [66].

401 As the temperatures at the early stages of the universe were well beyond the
402 critical temperature predicted by lQCD, it is thought that the universe was filled
403 with a QGP in the first few microseconds after the Big Bang [66]. Thus studying the
404 QGP is of interest to cosmologists, as it can give insight to the early universe and
405 its expansion, which is schematically represented in Figure 1.8. It is also postulated
406 that QGP formation occurs in the cores of neutron stars [67], giving another avenue
407 of interest for astrophysicists. Furthermore, studying the QGP and its properties can
408 help illuminate the dark, confounding corners of QCD that are not yet understood—
409 like confinement—making it an exciting subject of study for particle physicists. The
410 remainder of this section will discuss the theoretical characteristics of this interesting
411 plasma.

412 1.4.1 Properties of the QGP

413 1.4.1.1 Deconfinement

414 The most defining characteristic of the QGP is that the quarks and gluons within the
415 plasma are not confined inside hadrons, and instead interact as quasi-free particles. As
416 mentioned in Section 1.3.2.2, the coupling constant g_s becomes smaller with increasing
417 energies. At high enough energies, the coupling constant becomes small enough
418 that the quarks and gluons become deconfined. In lQCD, the order parameter for
419 deconfinement is the Polyakov loop expectation value **PolyakovLoop** $\langle L \rangle$, which
420 is zero in the confined phase and greater than zero in the deconfined phase. This
421 transition, from $\langle L \rangle = 0$ to $\langle L \rangle > 0$, is used²¹ to define the transition from hadronic

²⁰Though there are plenty of techniques to extend the lQCD results **TaylorSeries**, **ComplexDensity**, they are only applicable at small baryon densities.

²¹Technically the more common order parameter is the quark condensate discussed in the next section, but the critical temperatures predicted by lQCD using these different order parameters are usually very similar **QCDOOrderParameterSimilarity**.

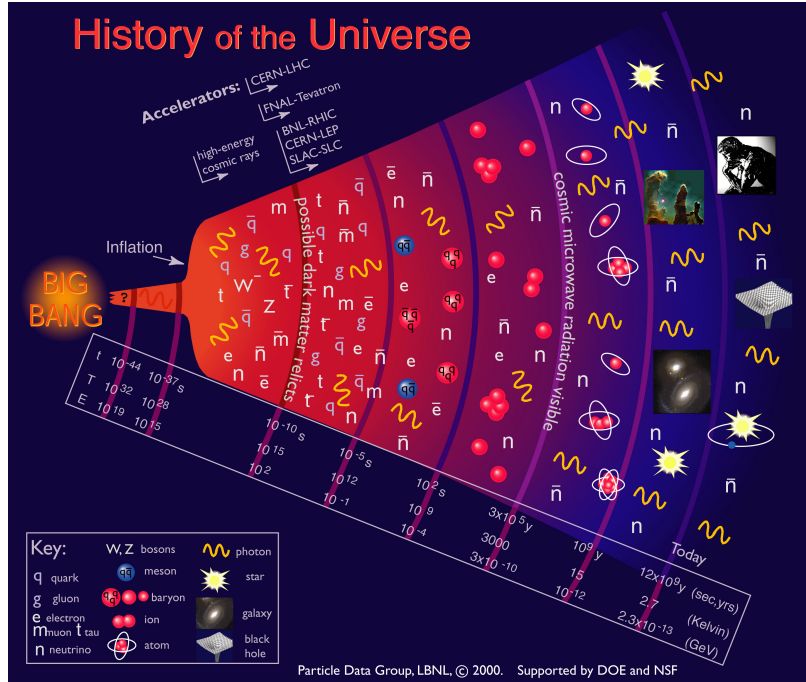


Figure 1.8: A schematic of the evolution of the universe, taken from [52]. The QGP phase of the universe on this diagram lies roughly between 10^{-10} and 10^{-5} seconds after the Big Bang.

422 matter to the QGP.

423 1.4.1.2 Chiral symmetry restoration

424 As mentioned in Section 1.3.2.3, the QCD vacuum has a non-zero quark condensate
 425 $\langle q\bar{q} \rangle$ which spontaneously breaks chiral symmetry. However, this non-zero condensate
 426 is the direct result of the confinement of QCD **TongGauge**. Thus, in the QGP—
 427 where the quarks and gluons are no longer confined—the quark condensate should
 428 vanish. As such, another defining characteristic of the QGP is the restoration of the
 429 spontaneously broken chiral symmetry of QCD, often referred to as **chiral symmetry**
 430 **restoration**. This transition, from $\langle q\bar{q} \rangle > 0$ to $\langle q\bar{q} \rangle = 0$, is also used to define the
 431 QGP phase transition.

432 An lQCD diagram of the deconfinement order parameter $\langle L \rangle$ and chiral symmetry
 433 order parameter $\langle q\bar{q} \rangle$ (along with their corresponding susceptibilities) as a function
 434 of the coupling $\beta = 6/g_s^2$ can be seen in Figure 1.9. Note that the susceptibilities
 435 are maximal at the same coupling value (corresponding to a critical temperature of

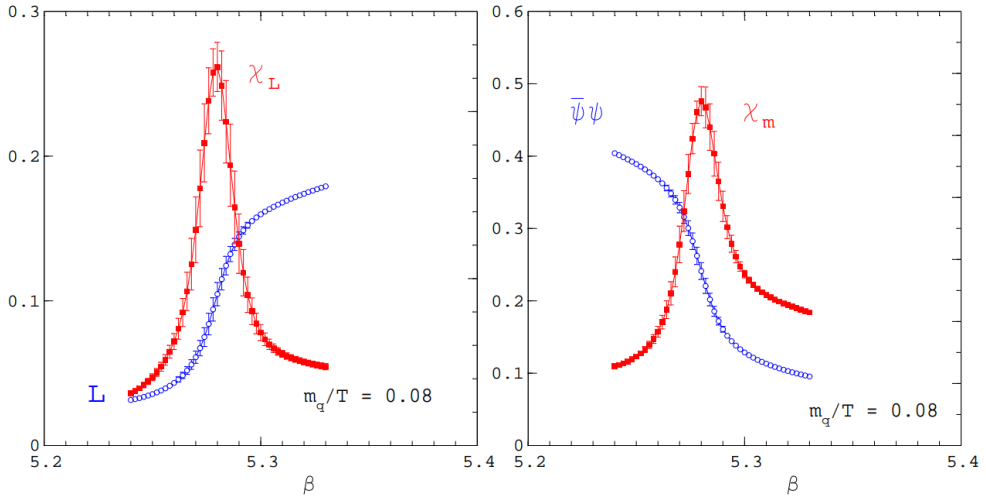


Figure 1.9: The deconfinement order parameter $\langle L \rangle$ and chiral symmetry order parameter $\langle q\bar{q} \rangle$ (along with their corresponding susceptibilities) as a function of the coupling $\beta = 6/g_s^2$ using 2-flavor 1QCD, taken from **FrithofLattice**. The critical temperatures (indicated by the maxima of the susceptibilities) occur at roughly $\beta = 5.28$, corresponding to a temperature of around 170 MeV.

436 around 170 MeV), indicating that both deconfinement and chiral symmetry restora-
 437 tion correspond to the same phase transition, namely the transition from hadronic
 438 matter to the QGP.

439 **1.4.1.3 Hydrodynamic behavior**

440 The QGP is a strongly interacting plasma. As such, it is expected to exhibit fluid-like
 441 behavior at a macroscopic level. Unfortunately, the calculation of QGP transport
 442 coefficients from first principles using QCD is very difficult **FlowViscPaper**. Us-
 443 ing perturbative techniques to calculate the shear and bulk viscosities of the QGP
 444 results in values that are an order of magnitude larger than those extracted from
 445 experimental data **Visc1**, **Visc2**. The extraction of these transport coefficients us-
 446 ing 1QCD is also challenging, as the aforementioned complex action problem makes
 447 it nearly impossible to simulate the QGP at non-zero baryon density. The most
 448 promising approach to calculating these transport coefficients is through the use of
 449 the AdS/CFT correspondence **AdSCFT**, which is a duality between a strongly cou-
 450 pled gauge theory (like QCD) and a weakly interacting gravitational theory (like
 451 string theory **StringTheory**). This approach has been used to approximate the

452 lower bound of the shear viscosity of a strongly-coupled medium **QGPViscADS**,

$$\eta/s \approx 1/4\pi, \quad (1.9)$$

453 which is often described as the shear viscosity of a “perfect fluid” **PerfectFluid**.
454 Experimental evidence suggests that the QGP has a shear viscosity that is very close
455 to this lower bound **QGPViscExp**, indicating that it is a nearly perfect fluid.

456 **1.4.1.4 Radiative energy loss**

457 Partons traveling through the QGP lose energy through both collisional and radiative
458 processes, as shown in Figure 1.10. The collisional energy loss is due to elastic
459 scattering between the partons and the constituents of the QGP. For a parton with
460 energy E much greater than its mass and the temperature of the QGP, the collisional
461 energy loss is given by **GluonRadiation**

$$\Delta E_{\text{coll}} \sim \alpha_s^2 T^2 L, \quad (1.10)$$

462 where T is the temperature of the QGP and L is the length of travel through the
463 medium (which is assumed to be larger than the critical length $L_{cr} \sim \frac{1}{\alpha_s T} \sqrt{\frac{E}{T}}$).
464 The radiative energy loss is due to gluon radiation induced by the presence of the
465 medium²². Again, for a parton with $E \gg M, T$, the radiative energy loss is given
466 by **GluonRadiation**

$$\Delta E_{\text{rad}} \sim \alpha_s^2 \sqrt{ET^3} L, \quad (1.11)$$

467 where E is the energy of the parton. As the radiative energy loss is proportional
468 to \sqrt{E} , it is the dominant energy loss mechanism for light, energetic partons (i.e.
469 u , d , and s quarks as well as gluons). However, gluons lose more energy than the
470 light quarks due to their larger color charge. The heavier quarks are expected to
471 lose less energy through radiative processes due to the *dead cone effect*, whereby the
472 gluon radiation is suppressed in the forward direction due to the larger masses of the
473 heavy quarks **DeadCone**. Even still, the radiative energy loss of heavy quarks is
474 larger than their collisional energy loss **DeadCone**, making radiative energy loss the
475 dominant energy loss mechanism for all energetic partons in the QGP.

²²Similar to bremsstrahlung, where electrically charged particles radiate photons in the presence of other charged particles.

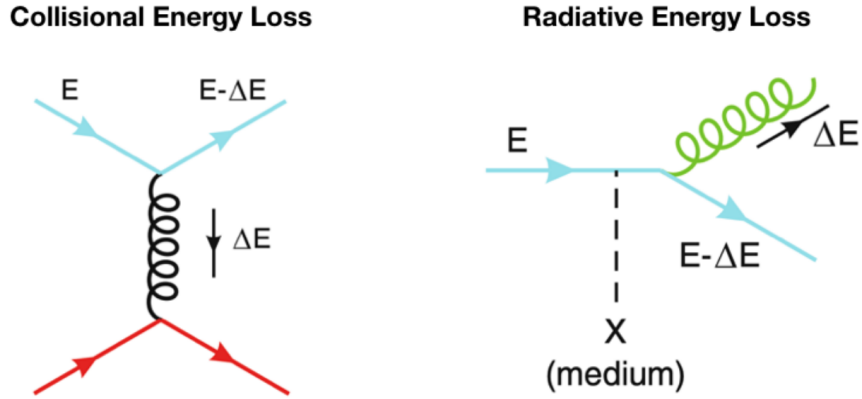


Figure 1.10: A diagram depicting the collisional (left) and radiative energy loss (right) processes of a parton traveling through the QGP. Radiative energy loss is the dominant energy loss mechanism for all energetic partons in the QGP.

476 1.4.2 Enhanced s -quark production

477 In the context of the research presented in this thesis, the most important characteristic
 478 of the QGP is the increase in the production of strange quarks relative to
 479 the production of up and down quarks [18]. Discovered in 1981 by physicists Johann
 480 Rafelski and Rolf Hagedorn, this *enhancement* in the production of strange quarks
 481 in the QGP is often referred to as **strangeness enhancement**. As mentioned in
 482 Section 1.3.2.5, strangeness is conserved during strong interactions. As such, the
 483 production of $s\bar{s}$ pairs can only come from four Feynman diagrams (to lowest order
 484 in pQCD), shown in Figure 1.11. A key insight made by Rafelski and Hagedorn is
 485 that in the QGP, the higher temperatures allow for the thermal production of $s\bar{s}$ pairs
 486 through gluon fusion ($gg \rightarrow s\bar{s}$ or diagrams (a) (b) and (c) in Figure 1.11). This gluon
 487 fusion occurs much faster than the quark-based production ($q\bar{q} \rightarrow s\bar{s}$ or diagram (d)
 488 in Figure 1.11), and allows for the full chemical equilibration of strangeness in the
 489 QGP in less than 10^{-24} seconds. Strangeness equilibration in a hadronic gas, on the
 490 other hand, takes much longer: on the order of 10^{-10} seconds [18].

491 1.4.2.1 Statistical hadronization

492 The production of strangeness in the QGP and within a hadron gas is often described
 493 in terms of the **statistical hadronization model** (SHM). The SHM is based off of

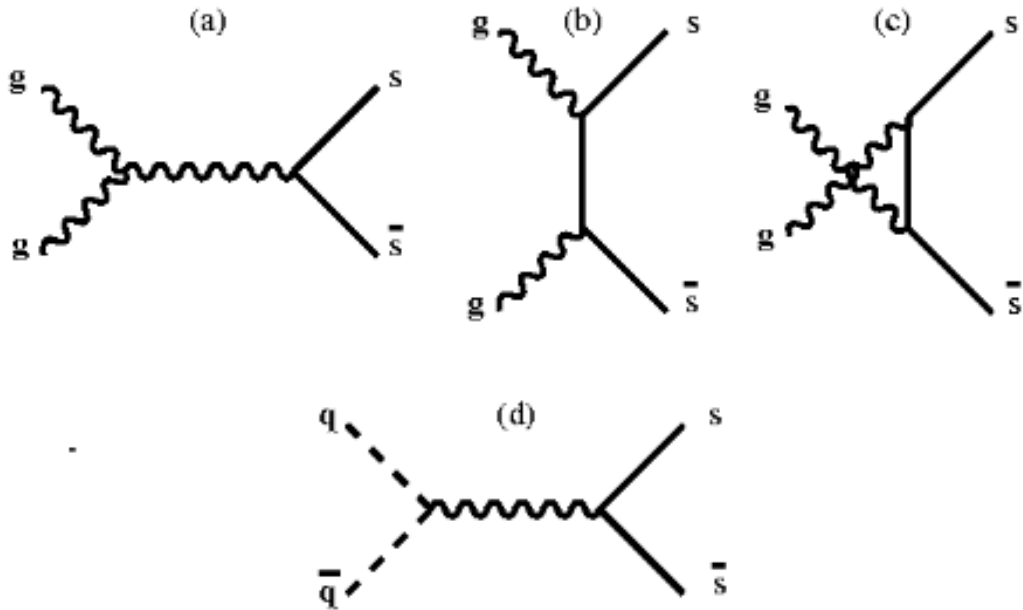


Figure 1.11: The four leading-order Feynman diagrams responsible for the production of $s\bar{s}$ pairs in the QGP, adapted from [18]. Diagrams (a), (b) and (c) are the gluon fusion processes, while diagram (d) is the quark-based process.

494 the Fermi model of hadron formation, where it is assumed that the strong interactions
 495 saturate the quantum particle production matrix elements **RafelskiStatisticalH**.
 496 This assumption allows for the calculation of the particle yields using only conser-
 497 vation laws and the available phase space, while ignoring the unknown microscopic
 498 details of the hadronization process. In the fundamental micro-canonical approach
 499 for the SHM, the available phase space is determined by the energy density of lo-
 500 calized “clusters” within the system. However, a grand canonical framework for the
 501 SHM is often used for highly energetic systems, where the phase space is determined
 502 by a global temperature-like parameter T .

503 The most important quantity for describing particle yields within the grand canon-
 504 ical SHM is the particle fugacity λ_i , which is defined as

$$\lambda_i = e^{\mu_i/T}, \quad (1.12)$$

505 where μ_i is the chemical potential of particle i . In essence, the fugacity “counts” the
 506 number of particles of type i in the system [18]. For systems in absolute chemical
 507 equilibrium, the chemical potentials for particle and anti-particle flavors are opposite

508 to each other. Consequently, the relationship between the particle and anti-particle
 509 fugacities is given by

$$\lambda_{\bar{i}} = \lambda_i^{-1}. \quad (1.13)$$

510 However, this relationship does not hold for systems that have not reached absolute
 511 chemical equilibrium, as the chemical potentials of the particle and anti-particle fla-
 512 vors are no longer opposite to each other. Due to the higher mass of the strange
 513 quark, the production of $s\bar{s}$ pairs usually proceeds at a much slower rate than the
 514 production of $u\bar{u}$ and $d\bar{d}$ pairs. As such, obtaining absolute chemical equilibrium for
 515 strange particles is difficult, especially in hadronic matter²³.

516 To account for this, the SHM introduces the concept of *relative* chemical equilib-
 517 rium, in which the strange phase space is not fully saturated, but whatever strangeness
 518 is produced is distributed among the strange hadron channels according to the law
 519 of maximum entropy **9212210·hep-ph**. This

520 : as mentioned in the previous section, the full chemical equilibration of strangeness
 521 in a hadron gas takes around

522 To describe the chemical equilibration of strangeness within the system, the SHM
 523 introduces two chemical factors, namely λ_s and γ_s . The factor λ_s is called the
 524 *strangeness fugacity*, and is defined as

$$\lambda_s = e^{\mu_s/T}, \quad (1.14)$$

525 where μ_s is the strangeness chemical potential. The strangeness fugacity ultimately
 526 describes the total abundance of strange quarks and anti-quarks

527 The factor λ_s is called the *strangeness suppression*, and is defined as

$$\lambda_s = \frac{2\langle n_{s\bar{s}} \rangle}{\langle n_{u\bar{u}} \rangle + \langle n_{d\bar{d}} \rangle}, \quad (1.15)$$

528 where $\langle n_{j\bar{j}} \rangle$ is the average number of quark-anti-quark pairs of flavor j . This factor
 529 describes the relative abundance of strange quarks and anti-quarks compared to up
 530 and down quarks and anti-quarks, and it approaches unity whenever the strange
 531 quarks are in *relative* chemical equilibrium with the u and d quarks.

532 The statistical hadronization model (SHM) is a theoretical framework that de-
 533 scribes the production of hadrons in high-energy nuclear collisions. It assumes that

²³As mentioned in the previous section, strangeness equilibration in a hadronic gas is over X times slower than in the QGP

534 hadrons are formed at the chemical freeze-out, when the system reaches a state of
535 thermal and chemical equilibrium. The SHM predicts that the abundance of hadrons
536 depends only on the available phase space and the conservation laws, and does not
537 depend on the details of the hadronization process.

538 One of the signatures of the quark-gluon plasma (QGP), a deconfined phase of
539 matter where quarks and gluons can move freely, is the strangeness enhancement.
540 This refers to the increased production of strange particles, such as kaons, lambdas,
541 and omegas, in QGP compared to normal hadronic matter. The strangeness en-
542 hancement can be explained by the fact that in QGP, strange quarks and antiquarks
543 are produced abundantly by gluon-gluon collisions, and they hadronize into strange
544 hadrons by recombination or evaporation. The SHM can account for the strangeness
545 enhancement by introducing a fugacity factor λ_s for each strange quark or antiquark,
546 which measures the deviation from chemical equilibrium.

547 The strangeness enhancement can be observed experimentally by comparing the
548 yields of strange particles in different colliding systems, such as proton-proton, proton-
549 nucleus, and nucleus-nucleus collisions. The SHM can fit the experimental data
550 by adjusting the parameters such as temperature, baryon chemical potential, and
551 strangeness fugacity. The SHM has been successful in describing the strangeness
552 enhancement at various energies, from SPS to LHC, and in different collision systems.

553 1.5 Using Heavy-Ion Collisions to Study the 554 QGP

555 The QGP phase diagram in Figure 1.7 shows two methods for producing the QGP:
556 increasing the system's temperature or increasing its baryon density. Luckily these
557 two methods are not mutually exclusive:

- 558 • Baryon density can be increased by looking at systems with a lot of baryons
559 packed together (like the nucleus of a lead atom)
- 560 • Temperature can be increased by smashing the aforementioned systems together
561 at higher energies (like in a particle accelerator)

562 Thus one of the best (and only) ways to study the QGP in a laboratory setting is
563 through relativistic **heavy ion collisions**: the smashing together of two heavy nuclei
564 at very high energies using a particle accelerator.

565 Unfortunately, producing the QGP in this manner has a major drawback; while
566 it is possible to heat up the system beyond the critical temperature required for
567 QGP formation, the system expands and cools *very* quickly. For example, the QGP
568 produced by colliding lead ions with center-of-mass energy $\sqrt{s_{\text{NN}}} = 2.76 \text{ TeV}$ at the
569 Large Hadron Collider (LHC) only lasts for around $3 \text{ fm}/c$ [68], or 10^{-23} seconds . A
570 diagram depicting the formation and evolution of the QGP in a heavy ion collision
571 can be seen in Figure 1.12. This diagram can be split up into the following stages:

572 1. The Lorentz-contracted nuclei approach each other at very high energies, and
573 the partons within the nuclei scatter off each other ($t = 0 \text{ fm}/c$).

574 2. As new partons are created from the initial scatterings, the energy density of
575 the system increases. Eventually this energy density is high enough to create
576 the QGP ($t \approx 1 \text{ fm}/c$).

577 3. Once the QGP is formed, it expands and cools in a hydrodynamic manner.

578 4. After the QGP cools below the critical temperature, the partons begin to
579 hadronize, resulting in the formation of a hadron gas ($t \approx 3 \text{ fm}/c$).

580 5. The hadron gas will continue to expand until the hadrons within the gas are no
581 longer strongly interacting with each other ($t \approx 10 \text{ fm}/c$). This is often broken
582 up into two stages:

- 583 • The hadrons cease to interact *inelastically*, called **chemical freeze-out**.
584 • The hadrons cease to interact *elastically*, called **kinetic freeze-out**.

585 6. If a detector is built within a few meters around the collision point, the final
586 state hadrons can be observed ($t \approx 10^{15} \text{ fm}/c$).

587 The last stage of this diagram is perhaps the most frustrating: it is only possible
588 to study the QGP by observing the final state hadrons. Luckily, there are some
589 key observables associated with those final state hadrons that can shed light on the
590 formation and evolution of this exciting plasma. Before those observables can be

discussed, however, it is necessary to introduce a key concept in heavy ion collisions:
 the centrality of the collision.

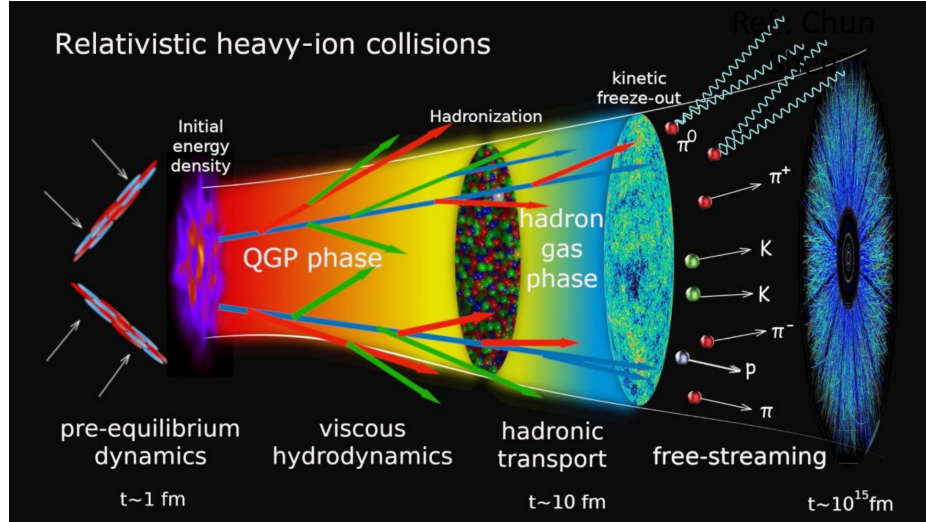


Figure 1.12: A schematic of the formation and evolution of the QGP in a heavy ion collision. The QGP is formed in the overlap region of the two colliding nuclei, and then expands and cools very quickly.

1.5.1 Collision centrality

The very first step of the heavy ion collision process involves the scattering of the partons within the two nuclei. However, these nuclei are not point-like objects: they have a finite size, and therefore need not collide “head-on”. Instead, the nuclei can collide at different **impact parameters** (commonly denoted as b), as shown in Figure 1.13. The impact parameter is defined as the distance between the centers of the two nuclei, measured in the transverse plane (the plane perpendicular to the initial directions of the nuclei). Collisions with a large impact parameter give rise to *spectator* nucleons, which do not participate in the collision and continue traveling as they please.

The impact parameter is very important when studying the QGP for a fairly straightforward reason: as the impact parameter decreases, the number of partonic scatterings increases, which in turn increases the energy density of the system. In some sense, the size of the impact parameter determines whether or not the QGP is formed in the subsequent stages of the collision. As such, characterizing heavy ion

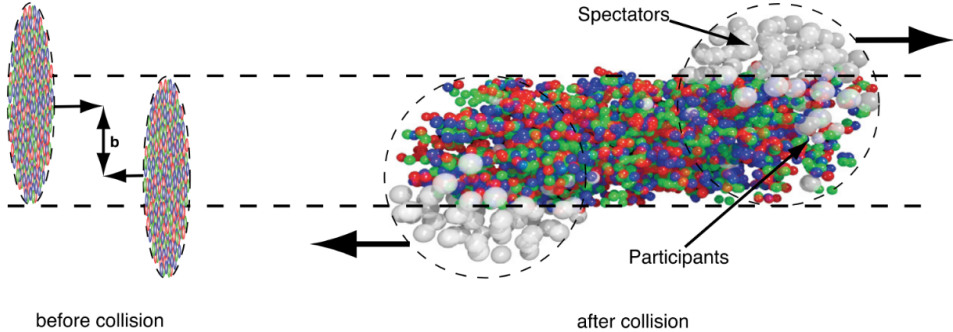


Figure 1.13: A schematic of a heavy ion collision with impact parameter b , taken from [69].

608 collisions by their impact parameter is quite useful. Unfortunately, much like the
 609 QGP, the impact parameter is not directly measurable and must be inferred from the
 610 final state hadrons.

611 Instead of classifying collisions based off their unobtainable impact parameter,
 612 they are instead classified by their **collision centrality**. The collision centrality is
 613 defined as

$$c = \frac{\int_0^b d\sigma/db' db'}{\int_0^\infty d\sigma/db' db'} = \frac{1}{\sigma_{AA}} \int_0^b \frac{d\sigma}{db'} db', \quad (1.16)$$

614 where σ_{AA} is the total cross section of the nucleus-nucleus (A-A) collision. As this
 615 number is strictly between 0 and 1, it is often expressed as a percentile: 0% corre-
 616 sponds to the most central collisions (lowest impact parameters), and 100% corre-
 617 sponds to the most peripheral collisions (highest impact parameters). If a monotonic
 618 relationship between b and the number of final state particles seen in the detector is
 619 assumed, the collision centrality can be experimentally determined [70]. The number
 620 of final state particles from a collision is called the **multiplicity** of the collision, and
 621 is often denoted as N_{ch} . The subscript ch indicates that only charged particles are
 622 counted, as neutral particles are not seen by most detectors.

623 In practice, the collision centrality percentiles are usually determined by looking
 624 at the distribution of events as a function of the signal (effectively N_{ch}) as measured
 625 by a particular detector. The percentile for a specific event can then be determined
 626 by integration:

$$c \approx \frac{1}{\sigma_{AA}} \int_{N_{ch}}^{\infty} \frac{d\sigma}{dN'_{ch}} dN'_{ch}, \quad (1.17)$$

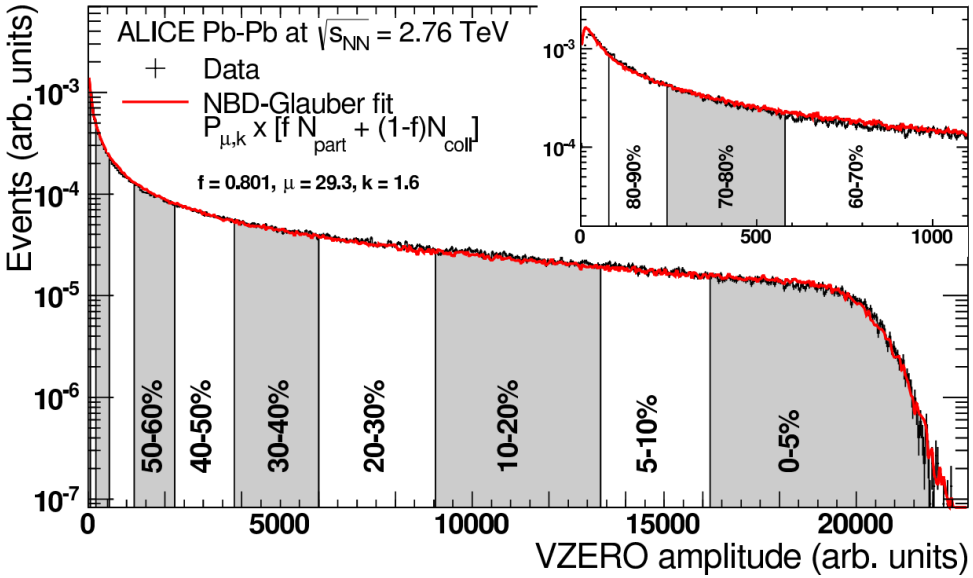


Figure 1.14: The distribution of Pb–Pb collision events as a function of event activity in the ALICE VZERO detector, taken from [71].

where N_{ch} is the multiplicity of the event in question. An example of separating events into centrality percentiles using this method can be seen in Figure 1.14. In this plot, Pb–Pb collisions are characterized by their event activity in the ALICE VZERO detector (which will be discussed in more detail in the next chapter). The red points correspond to fits obtained using Monte Carlo simulations based off of the Glauber model [70], [71]. The Glauber model [72] is a geometric model that treats the nuclei as a collection of nucleons, and models the collisions as a superposition of binary nucleon-nucleon collisions. This model gives a relationship between the impact parameter b , the number of participating nucleons N_{part} , and the number of binary nucleon-nucleon collisions N_{coll} . While not of particular import to this thesis, fitting the Glauber model to the data actually allows for the determination of the impact parameter corresponding to a given multiplicity percentile. The fact that the model describes the data well also serves as a sanity check for the experimental estimation of the collision centrality. In this thesis, the terms “multiplicity percentile” and “collision centrality” will be used interchangeably.

The approximation given by Equation 1.17 has an additional benefit: it allows for the determination of centrality without a clearly defined impact parameter. This

644 is useful for proton-proton and proton-lead collisions, where the impact parameter is
645 ill-defined.

646 1.6 Experimental signatures of QGP formation

647 As mentioned in Section 1.5, the QGP produced within a heavy ion collision is *very*
648 short lived. As such, any attempt to study the QGP and its formation must be
649 done using the detector-accessible final state hadrons. Luckily there are a number of
650 signatures that can be used to study the QGP in experiment, including

- 651 • **jet quenching** [73], where the energy of a jet is heavily reduced due to its
652 interactions with the QGP,
- 653 • **collective flow** [74], where the motion of the partons within the QGP is heavily
654 influenced by the overall fluid-like medium, and
- 655 • **strangeness enhancement** [18], where the QGP exhibits an increase in the
656 production of strange quarks relative to up and down quarks.

657 These signatures are discussed in more detail in the following sections.

658 1.6.1 Jet quenching

659 The high momentum partons produced in the initial hard scatterings of heavy ion
660 collisions often traverse the QGP medium. Much like electron tomography, where the
661 passage of electrons through an atomic medium can give insight to the structure of the
662 atoms within, these high momentum partons can be used to probe the QGP. These
663 colored partons interact with the colored medium, losing energy in the process. As
664 discussed in Section 1.3.2.4, these partons are never observed individually; instead,
665 they hadronize into a spray of particles known as a jet. Thus the energy lost by
666 the parton is not observed directly, but rather as a reduction in the energy of the
667 resulting jet. This phenomenon is known as **jet quenching**, and is one of the most
668 well studied signatures of QGP formation.

669 Experimentally, this quenching is observed by studying *dijets*. While the term
670 “jet” refers to a single spray of particles observed in the detector, the initial hard
671 scattering responsible for the formation of the jet corresponds to the production of

672 two high momentum partons. Traveling in opposite directions in the transverse plane,
 673 these partons often produce two jets that are back-to-back in φ (the azimuthal angle
 674 in the transverse plane). These two jets are collectively referred to as a dijet. In pp
 675 collisions, the energy of the two jets is roughly equal as the corresponding partons
 676 don't lose energy to a medium. In heavy ion collisions, however, the partons lose
 677 energy to the QGP due to gluon radiation and elastic scattering with the medium's
 678 constituents [75]. If one of the two partons has a larger path length through the
 679 QGP, it will lose more energy than the other parton, resulting in an imbalance in the
 680 energy of the two jets. A schematic of this process for pp and A–A collisions can be
 681 seen in Figure 1.15.

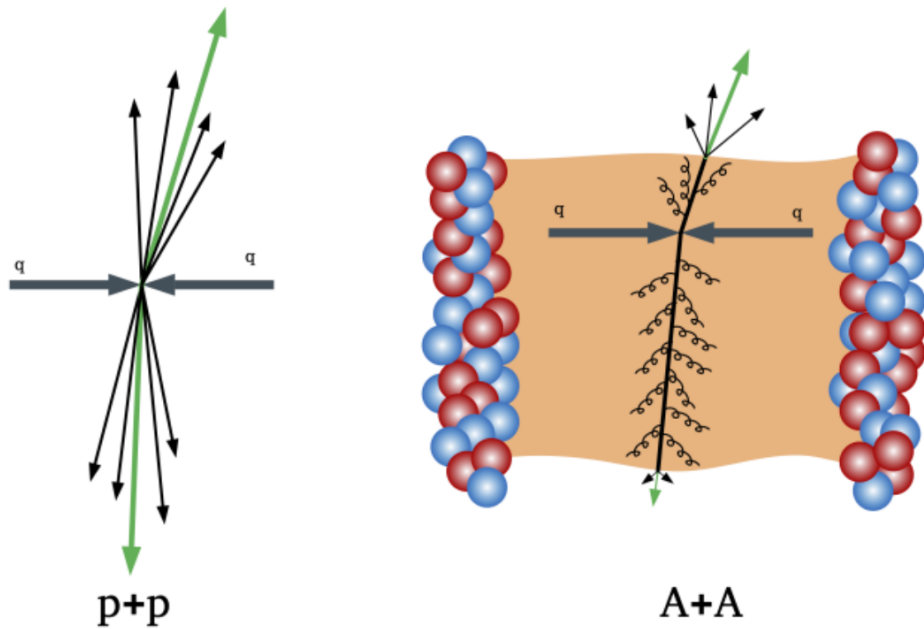


Figure 1.15: A schematic of the formation of dijets in pp and A–A collisions, taken from [76].

682 However, the path length within the QGP of the dijet-forming partons should be
 683 roughly uniform, washing out this assymetry over a large event sample. As such, jet
 684 quenching is experimentally observed by selecting high momentum “trigger” hadrons,
 685 which most likely originated from the parton with the smaller QGP path length. The
 686 jet corresponding to this higher momentum trigger—referred to as the “near-side” jet—
 687 is then compared with its partner jet, which would be 180° away in azimuth—called

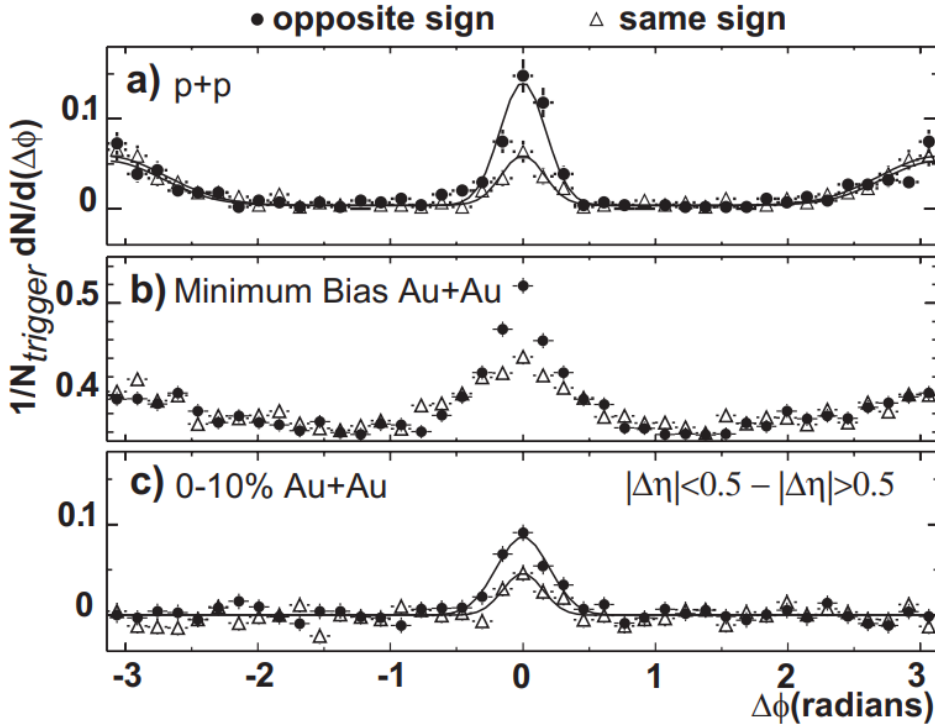


Figure 1.16: Hadron yields corresponding to the near-side jet (near $\Delta\varphi = 0$) and the away-side jet ($\Delta\varphi = \pm\pi$), taken from [77]. In pp and minimum bias Au–Au collisions, the away-side jet is present. However, at high centrality (0–10%), the away-side jet completely disappears.

the “away-side” jet. The first collaboration to observe this jet quenching was the STAR collaboration at the Relativistic Heavy Ion Collider (RHIC) [77]. By looking at high transverse momentum hadrons produced in Au–Au collisions, they found that the away-side jet began to “disappear” as the centrality of the collision increased, as shown in Figure 1.16. This disappearance is due to the away-side jet losing energy to the QGP, such that the corresponding hadrons in the away-side fall below the momentum cutoff.

1.6.2 Collective flow

The QGP is a strongly interacting medium, whose constituent partons are heavily coupled to their surroundings. Just as the pebbles within a river get swept up in the flow of the water, the partons within the QGP are influenced by the flow of this

699 medium. This flow manifests itself by the presence of collective effects in the final
 700 state hadrons, which are often quantified using **collective flow** components. These
 701 flow components are obtained by expanding the final state hadron distribution in a
 702 Fourier series with respect to the azimuthal angle ϕ [78],

$$E \frac{d^3 N}{d^3 p} = \frac{1}{2\pi} \frac{d^2 N}{p_t dp_t dy} \left(1 + \sum_{n=1}^{\infty} 2v_n \cos[n(\phi - \Psi_R)] \right), \quad (1.18)$$

703 where E is the energy of the particle, p is its momentum, p_T is the momentum
 704 component in the plane transverse to the beam axis, y is the particle's rapidity, and
 705 Ψ_R is the reaction plane angle. This reaction plane angle is defined by the beam axis
 706 and the impact parameter vector. The Fourier coefficients

$$v_n = \langle \cos[n(\phi - \Psi_R)] \rangle \quad (1.19)$$

707 determine the “strength” of the corresponding flow component. The first two co-
 708 efficients, v_1 and v_2 , are referred to as **directed (radial) flow** and **elliptic flow**,
 709 respectively. A non-zero directed flow originates from the space-momentum correla-
 710 tions in particle production from a longitudinally slanted source [79]. Directed flow
 711 is often much smaller than elliptic flow (by over an order of magnitude) [80], but it
 712 can still effect some of the measurements presented in this thesis (see Section ?? for
 713 more details).

714 Elliptic flow characterizes the anisotropy of the particle production in the trans-
 715 verse plane. This anisotropy is believed to be caused by the initial anisotropy of the
 716 collision geometry, where the overlap region of the colliding nuclei forms an “almond”
 717 shape. This almond is where the initial QGP is formed, which then hydrodynamically
 718 expands and thermalizes nearly instantaneously. The initial spacial anisotropy results
 719 in unequal QGP path lengths for the constituent partons, which ultimately results in
 720 an anisotropic momentum distribution for the corresponding hadrons (i.e. partons
 721 which travel through more medium lose more energy, as discussed in Section 1.6.1).
 722 A diagram depicting this process can be seen in Figure 1.17.

723 1.6.2.1 Avoiding Ψ_R

724 Reconstructing the reaction plane angle Ψ_R is difficult as it must be done on an event-
 725 by-event basis [78]. As such, it is often more convenient to measure the collective

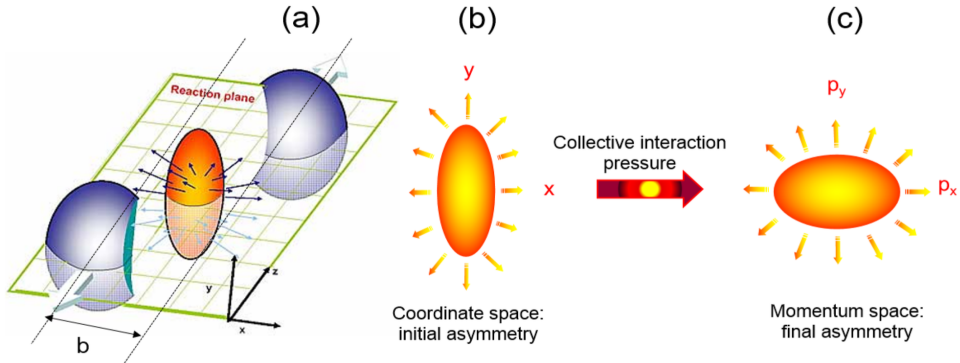


Figure 1.17: A schematic of the formation of elliptic flow in a heavy ion collision. The initial anisotropy in coordinate space results in a pressure gradient that causes a momentum space anisotropy in the final state hadrons.

726 flow components by looking at two-particle correlations in the azimuthal angle ϕ . In
 727 other words, the flow components can be obtained by looking at the distribution of
 728 pairs of particles as a function of $\Delta\phi = \phi_1 - \phi_2$, where ϕ_1 and ϕ_2 are the azimuthal
 729 angles of two (non-identical) particles. This distribution can be decomposed into a
 730 Fourier series similar to Equation 1.18 [81],

$$\frac{dN^{\text{pair}}}{d\Delta\varphi} = a_0 + 2a_1 \cos \Delta\varphi + 2a_2 \cos 2\Delta\varphi + \dots, \quad (1.20)$$

731 where $v_n \equiv a_n/a_0$ are the very same flow coefficients from before. This bypasses the
 732 need to reconstruct the reaction plane angle Ψ_R , but it also makes clear that any
 733 analyses involving two-particle angular correlations (like the one presented in this
 734 thesis) must be mindful of the presence of these coefficients (see Chapter ?? for more
 735 details).

736 1.6.3 Strangeness enhancement

737 Experimentally, strangeness production is measured by looking at the abundance
 738 of strange hadrons relative to non-strange hadrons, like pions. For central heavy
 739 ion collisions—both at the LHC and RHIC—these strange/non-strange particle ratios
 740 are found to be consistent with a hadron gas in both thermal *and* chemical equilib-
 741 rium [82], [83]. As mentioned previously, this is a strong indication that the QGP
 742 is formed in these collisions. Furthermore, these particle ratios as measured in lower

743 multiplicity pp collisions at the LHC are found to be consistent with statistical mod-
744 els *without* chemical equilibration [84], [85]. Under the strangeness enhancement
745 picture, this indicates that QGP formation does *not* occur in these lower multiplicity
746 pp collisions.

747 However, filling in the gaps between low multiplicity pp collisions and high multi-
748 plicity Pb–Pb collisions reveals a more complicated picture, as shown in Figure 1.18.
749 The particle ratios seem to be consistent with a smooth transition between the two
750 regimes, independent of collision system. In other words, the ratios in higher multi-
751 plicity pp and p–Pb collisions match up nicely with the ratios in lower multiplicity
752 Pb–Pb collisions. This indicates that the enhanced production of strange quarks is
753 not exclusive to heavy ion collisions; there is an “onset” of strangeness enhancement
754 occurring in lower multiplicity pp and p–Pb collisions. Furthermore, this enhancement
755 is seen to scale with the number of strange quarks in the hadron: the Ω baryon (sss)
756 exhibits the largest enhancement, while the proton (uud) sees virtually no increase.
757 This provides even stronger evidence for the formation of a chemically equilibrated
758 QGP, which no longer appears exclusive to heavy ion collisions.

759 While extensions to the aforementioned statistical models can describe these
760 multiplicity-dependent particle ratios in a phenomenological manner [87], the mi-
761 croscopic origins of this enhancement are not well understood. By investigating the
762 production of strange hadrons in p–Pb collisions (where the onset is greatest), this
763 thesis aims to shed light on the origins of this strange enhancement. However, it is
764 necessary to first introduce some theoretical models to help interpret the results of
765 this thesis.

766 1.7 Heavy-Ion Collision Models

767 Theoretical models of heavy ion collisions are pertinent to the understanding of QCD
768 and the QGP. Without them, there would be no framework for interpreting the results
769 from the very expensive experiments dedicated to studying this strongly interacting
770 plasma. Unfortunately, due to the complexity of these heavy ion collision systems,
771 there is no *single* model that can describe the entire collision evolution. Instead,
772 the choice of model to compare a particular observable to depends very heavily on
773 the observable in question. For example, some models treat the QGP phase of the

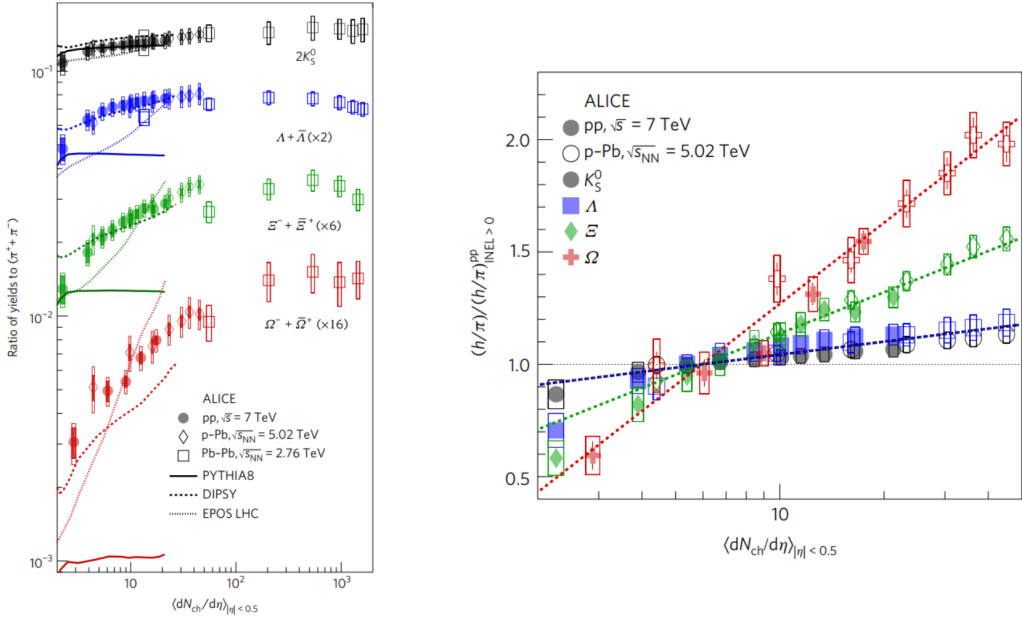


Figure 1.18: The particle ratios of strange hadrons to pions as a function multiplicity for different collision systems (left) and those same ratios normalized to an inclusive pp sample (right). The ratios appear to only depend on the multiplicity of the collision, and not the collision system. Taken from [86].

774 collision as a hydrodynamic system, washing out information about the initial par-
 775 tonic scatterings [88]. This can be useful when trying to study bulk properties of
 776 the QGP (like the v_2 from Section 1.6), but not-so-useful when studying jets and
 777 their constituents. Other models focus more on the individual partonic scatterings
 778 and subsequent hadronization, but do not include an explicit QGP phase [89], [90].
 779 Such models are powerful tools for analyzing smaller collision systems (pp and lower
 780 multiplicity p–Pb), but fail to capture many of the features observed in heavy ion
 781 collision data. In this section, the models used to help interpret the results of this
 782 thesis will be discussed. All of these models are capable of simulating pp, p–Pb, and
 783 Pb–Pb events.

784 1.7.1 PHSD

785 Parton-Hadron-String-Dynamics (PHSD) [91], [92] is the only model explored in this
 786 thesis that utilizes a **microscopic transport approach**: it simulates the full space-
 787 time evolution of a heavy-ion collision by modeling the interactions of individual

788 particles. Here “particles” refers to different quantities (strings, partons, hadrons)
 789 which are all evolved in different ways. The transport equations of the partons and
 790 hadrons are derived from the Kadanoff-Baym (KB) equations [93], which describe
 791 the non-perturbative transport of particles in a strongly interacting system. The
 792 evolution of a collision within PHSD is as follows.

793 1.7.1.1 Initial stages

794 Prior to the collision, the simulation is broken up into a 3D-grid of size 56 in each
 795 of the x, y, and z directions. The total size of the grid increases with each time step
 796 such that the number of particles within a given cell evolves smoothly with time. The
 797 initial momentum distribution and abundances of partons within the nuclei (prior to
 798 any collision) are given by the thermal distributions

$$f(\omega, \vec{p}) = C_i p^2 \omega \rho_i(\omega, \vec{p}) n_{F/B}(\omega/\tau), \quad (1.21)$$

799 where ρ_i are the spectral functions of the quarks and gluons ($i = q, \bar{q}, g$) and $n_{F/B}$ are
 800 the Fermi-Dirac (for quarks) and Bose-Einstein (for gluons) distributions. Once the
 801 nuclei collide, the partons interact with each other under the Lund string model to
 802 form *leading hadrons* (at large rapidity) and *pre-hadrons* (at midrapidity), as shown
 803 in Figure 1.19. The leading hadrons are immune to dissociation within the QGP,
 804 while the pre-hadrons are not.

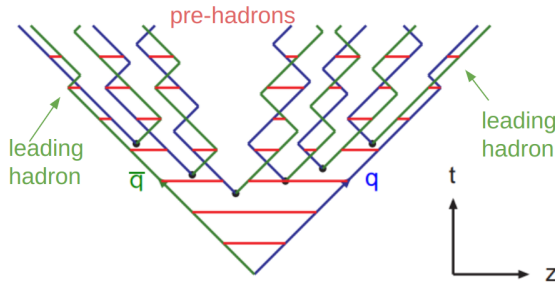


Figure 1.19: The Lund string model, with pre-hadrons and leading hadrons labeled.

805 1.7.1.2 QGP phase

806 If the energy density ϵ of a given cell increases beyond the critical energy density
 807 $\epsilon_c = 0.5 \text{ GeV/fm}^3$, the pre-hadrons within that cell are dissolved into partons. The

808 partons are then treated as interacting quasi-particles under the DQPM [94] model,
 809 with Lorentzian spectral functions given by

$$\rho_j(\omega) = \frac{\gamma_j}{E_j} \left(\frac{1}{(\omega - E_j)^2 + \gamma_j^2} - \frac{1}{(\omega + E_j)^2 + \gamma_j^2} \right) \quad (1.22)$$

810 where i is one of (q, \bar{q}, g) and the width γ_i is given by

$$\gamma_g(T) = N_c \frac{g^2 T}{8\pi} \ln \frac{2c}{g^2}, \quad \gamma_q(T) = \frac{N_c^2 - 1}{2N_c} \frac{g^2 T}{8\pi} \ln \frac{2c}{g^2}, \quad (1.23)$$

811 where T is the temperature (calculated from the energy density within a given cell).
 812 This is the key difference between DQPM and other transport models—the quarks and
 813 gluons have non-zero temperature-dependent widths in the medium! The coupling
 814 constant g is also temperature dependent, and is of the form

$$g^2(T/T_c) = \frac{48\pi^2}{(11N_c - 2N_f) \ln(\lambda^2(T/T_c - T_s/T_c)^2)}. \quad (1.24)$$

815 The parameters T_s and λ are fit to lattice QCD (lQCD) results [92]. The spectral
 816 functions are enough to describe the propagation of the mean-fields of the partons
 817 (effectively their Greens functions) via the aforementioned KB equations. The col-
 818 lisional terms in these equations are determined by the modified scattering cross
 819 sections of the partons. These cross sections are calculated using the leading order
 820 Feynman diagrams, with the DQPM-modified quark and gluon propagators given by

$$i\delta_{ij} \frac{q + M_q}{q^2 - M_q^2 + 2i\gamma_q q_0} \quad (1.25)$$

821 and

$$-i\delta_{ab} \frac{g^{\mu\nu} - q^\mu q^\nu/M_g^2}{q^2 - M_g^2 + 2i\gamma_g q_0}, \quad (1.26)$$

822 respectively. Due to the large masses of the gluons, $q + \bar{q} \rightarrow g + g$ and $g \rightarrow g + g$ are
 823 suppressed and thus not included in the model.

824 1.7.1.3 Hadronization

825 Whenever the energy density of a given cell falls below the aforementioned critical
 826 energy density ($\epsilon_c = 0.5$ GeV/fm 3), the partons within begin to hadronize. The

827 dynamical hadronization of partons into hadrons is modeled by the equations

$$\frac{dN_m(x, p)}{d^4x d^4p} = \text{Tr}_q \text{Tr}_{\bar{q}} \delta^4(p - p_q - p_{\bar{q}}) \delta^4\left(\frac{x_q + x_{\bar{q}}}{2} - x\right) \\ \times \omega_q \rho_q(p_q) \omega_{\bar{q}} \rho_{\bar{q}}(p_{\bar{q}}) |v_{q\bar{q}}|^2 W_m(x_q - x_{\bar{q}}, (p_q - p_{\bar{q}})/2) \\ \times N_q(x_q, p_q) N_{\bar{q}}(x_{\bar{q}}, p_{\bar{q}}) \delta(\text{flavor, color}). \quad (1.27)$$

828 for mesons and

$$\frac{dN_B(x, p)}{d^4x d^4p} = \text{Tr}_{q_1} \text{Tr}_{q_2} \text{Tr}_{q_3} \delta^4(p - p_{\xi_3}) \delta^4(x - \xi_3) \delta\left(\sqrt{(\tau_1 - \tau_2)^2}\right) \\ \times \omega_{q_1} \rho_{q_1}(p_1) \omega_{q_2} \rho_{q_2}(p_2) \omega_{q_3} \rho_{q_3}(p_3) \\ \times |M_{qqq}|^2 W_B(\xi_1, \xi_2, p_{\xi_1}, p_{\xi_2}) \\ \times N_{q_1}(x_1, p_1) N_{q_2}(x_2, p_2) N_{q_3}(x_3, p_3) \delta(\text{flavor, color}). \quad (1.28)$$

829 for baryons. The terms for the meson case are described as follows:

- 830 • Tr_q is shorthand notation for $\text{Tr}_q = \sum_q \int d^4x_q \int \frac{d^4p_q}{(2\pi)^4}$, where q is summed over
831 all spin, color, and flavor degrees of freedom.
- 832 • $\delta^4(p - p_q - p_{\bar{q}})$ forces conservation of four-momentum. Note that the quarks
833 and anti-quarks are allowed to be off-shell (due to their non-zero widths), thus
834 this can result in off-shell mesons.
- 835 • $\delta^4\left(\frac{x_q + x_{\bar{q}}}{2} - x\right)$ puts the resulting meson in-between the quark and anti-quark
836 pair.
- 837 • ω_q and $\omega_{\bar{q}}$ are the energies of the quark and anti-quark, respectively.
- 838 • $\rho_q(p_q)$ and $\rho_{\bar{q}}(p_{\bar{q}})$ are the aforementioned spectral functions of the quark and
839 anti-quark, respectively.
- 840 • $|v_{q\bar{q}}|^2$ is the DQPM-determined *effective quark-anti-quark interaction*, which is
841 shown as the green dashed line in Figure 1.20. Note that this value is very small
842 for large quark (energy) densities, and thus this entire equation is effectively
843 zero. However, for low quark densities this value blows up, which “turns on” the
844 hadronization (and also guarantees that all partons will hadronize *eventually*).
- 845 • $W_m(x_q - x_{\bar{q}}, (p_q - p_{\bar{q}})/2)$ is the phase-space distribution of the resulting (pre-
846)meson

- 847 • $N_q(x_q, p_q)$ and $N_{\bar{q}}(x_{\bar{q}}, p_{\bar{q}})$ are the phase-space densities of the quark and anti-
 848 quark, respectively.
- 849 • $\delta(\text{ flavor, color })$ is shorthand for “make sure flavor quantum numbers are con-
 850 served and that the resulting meson is color-neutral”.

851 The terms for the baryon case are similar.

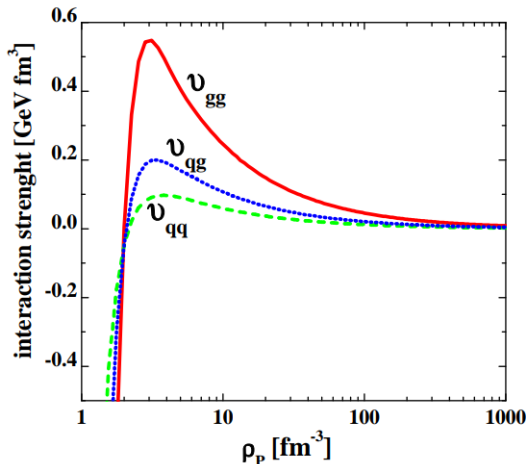


Figure 1.20: The effective quark-quark (green), quark-gluon (blue), and gluon-gluon (red) interactions as a function of parton density in DQPM, taken from [91].

852 The numerical integrations of equations 1.27 and 1.28 for a fixed test parton
 853 ultimately give the probability for a hadronization event to occur. From there, events
 854 are randomly selected using Monte Carlo techniques, which give a color neutral state
 855 with definite x , p and flavor. However, this is *still* not enough to specify a hadron
 856 completely: many hadronic states of the same flavor have large widths. Thus to
 857 determine the identity of the final hadron, the weight of each possible²⁴ hadronic
 858 spectral function is computed. The hadron is then randomly assigned an identity
 859 based on these weights using Monte Carlo.

²⁴PHSD only includes the baryon octet/decouplet, the spin 0 and spin 1 meson nonets, and a few higher resonance states. Furthermore, if the invariant mass of the color neutral state is above 1.3 GeV (for mesons) or 1.5 GeV (for baryons), the state is treated as a Lund string with further decay handled by the JETSET algorithm [95]

860 **1.7.1.4 Hadronic phase**

861 All of the hadrons produced in the previous steps are transported using Hadron-
 862 String-Dynamics [96] (PHSD without the P). The phase-space distributions of the
 863 hadrons in HSD are transported using the equation

$$\begin{aligned} & \left\{ \left(\Pi_\mu - \Pi_\nu \partial_\mu^p U_h^\nu - M_h^* \partial_\mu^p U_h^S \right) \partial_x^\mu + \left(\Pi_\nu \partial_\mu^x U_h^\nu + M_h^* \partial_\mu^x U_h^S \right) \partial_p^\mu \right\} f_h(x, p) \\ &= \sum_{h_2 h_3 h_4 \dots} \int d2d3d4 \dots [G^\dagger G]_{12 \rightarrow 34 \dots} \delta_\Gamma^4(\Pi + \Pi_2 - \Pi_3 - \Pi_4 \dots) \\ & \quad \times \left\{ f_{h_3}(x, p_3) f_{h_4}(x, p_4) \bar{f}_h(x, p) \bar{f}_{h_2}(x, p_2) \right. \\ & \quad \left. - f_h(x, p) f_{h_2}(x, p_2) \bar{f}_{h_3}(x, p_3) \bar{f}_{h_4}(x, p_4) \right\} \dots, \end{aligned} \quad (1.29)$$

864 where U_h^S and U_h^μ are the scalar and vector hadron self-energies, respectively. The
 865 effective mass of the hadron M_h^* is given by

$$M_h^* = M_h + U_h^S, \quad (1.30)$$

866 and its effective momentum is given by

$$\Pi^\mu = p^\mu - U_h^\mu. \quad (1.31)$$

867 The “collisional” term $[G^\dagger G]_{12 \rightarrow 34 \dots}$ is the transition rate for the process $1 + 2 \rightarrow$
 868 $3 + 4 + \dots$, which is modeled using Lund string fragmentation. The self-energies U_h^S
 869 and U_h^μ are evaluated on the basis of a Nambu-Jona-Lasinio (NJL)-type model [97]
 870 for the QCD Lagrangian. Once these self-energies (and $[G^\dagger G]_{12 \rightarrow 34 \dots}$) are specified,
 871 the transport equation (Equation 1.29) can be solved.

872 **1.7.1.5 A simple overview**

873 While the equations that govern PHSD are quite complicated, the overall picture is
 874 relatively simple. It can be summarized as follows:

- 875 • First, the simulation is split up into cells whose sizes evolve with time, as shown
 876 in Figure 1.21.
- 877 • As the initial nuclei collide, and the interacting partons form pre-hadrons and
 878 leading hadrons.

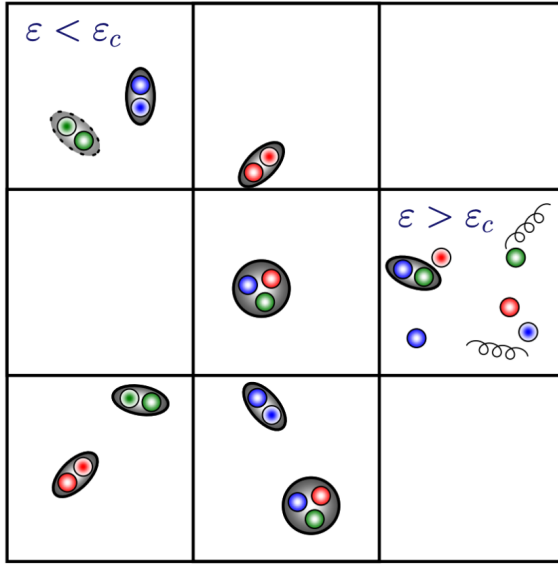


Figure 1.21: The cells within PHSD. If the energy density of the cell is greater than the critical energy density, the pre-hadrons dissolve into partons.

- 879 • If the energy density of a cell is too high, the pre-hadrons dissolve into partons,
880 which are handled by the DQPM model.
- 881 • If a cell with partons in it cools off, the partons dynamically hadronize.
- 882 • The resulting hadrons (and any hadrons present in a particular cell) are trans-
883 ported using HSD.

884 1.7.2 EPOS LHC

885 In the EPOS LHC [98] model, the initial colliding nuclei results in many parton-
886 parton scatterings happening in parallel, as shown in Figure 1.22. These simultaneous
887 scatterings form a parton ladder, which are modeled as relativistic Lund strings. Long
888 before hadronization, the model separates into two distinct parts: the *core* and the
889 *corona*. This designation is based on the string density (i.e. the number of string
890 segments per unit volume). If the string density exceeds a critical density ρ_c , the
891 string segments are considered to be in the core. Otherwise, they are in the corona.
892 The core is evolved in a hydrodynamic manner, which loses all information about
893 the initial string segments and their interactions. Hadronization in the core is handled

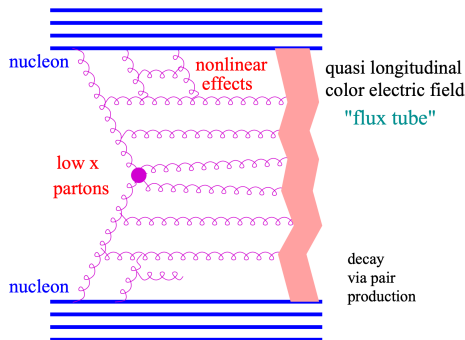


Figure 1.22: A schematic of the elementary interaction in EPOS LHC in which many parton-parton interactions are occurring simultaneously [98].

894 by a microcanonical procedure known as Cooper-Frye freeze-out, which is described
 895 in detail in [99]. The core is associated with the QGP medium, and dominates particle
 896 production at higher multiplicities. The corona, however, corresponds to unmodified
 897 Lund string fragmentation, which dominates at large rapidity and in lower multiplicity
 898 events.

899 1.7.3 DPMJET

900 Perhaps the most simple²⁵ event generator explored in this thesis is the DPMJET [100]
 901 model. DPMJET combines the Dual Parton Model (DPM) [101] with the Lund string
 902 model [59] to describe proton-proton, proton-nucleus, and nucleus-nucleus collisions
 903 across a large range of energies. The DPM describes all of the soft, non-perturbative
 904 multi-particle events that occur within a heavy ion collision using various large N_c
 905 and N_f limits of QCD. This is the only model explored in this thesis that does
 906 not have an explicit QGP phase, as the collision constituents²⁶ are always treated
 907 independently. Thus DPMJET serves as a good baseline for vacuum fragmentation,
 908 and can be compared with other models (and data) to help quantify the effects of the
 909 explicit QGP phase.

²⁵Still *extremely* complicated from a theoretical perspective, but has the least moving parts.

²⁶Strings. It's always strings.

Chapter Two: Summary and outlook

911 Quantum chromodynamics (QCD) is the theory that describes how the protons and
912 neutrons, which compose almost all ordinary matter, are bound to one another within
913 the nucleus of an atom. In this theory, the fundamental constituents of matter are
914 *not* protons and neutrons, but rather quarks and gluons. These quarks and gluons
915 bind together through their color charge, creating the color neutral hadrons observed
916 in nature. One of the most interesting predictions of QCD is that, at extreme temper-
917 atures and densities, these hadrons dissolve into their constituent quarks and gluons,
918 forming a new state of matter known as the Quark-Gluon Plasma (QGP). Under-
919 standing the QGP, which is thought to be the state of the universe shortly after the
920 Big Bang, can help answer questions about the nature of everyday matter and the
921 evolution of the universe.

922 Studying the QGP requires recreating the extreme conditions of the early uni-
923 verse, which can only be achieved through high energy particle collisions. In such
924 collisions, however, the QGP is only produced for a very short time, after which it
925 expands and cools into the hadrons that are observed in the detector. Thus the QGP
926 cannot be studied directly, and its formation and properties must be inferred from
927 the information that is accessible to experiment. One of the first predicted exper-
928 imental signatures for the formation of this plasma is the enhancement of strange
929 hadron production, relative to non-strange pion production. While this enhancement
930 was thought to be unique to heavy-ion collisions, experimental data from ALICE
931 indicates that even high multiplicity pp and p–Pb collisions exhibit an onset of this
932 enhanced production. This enhancement can only be described using statistical mod-
933 els, as its microscopic origin is not yet understood.

934 One way to study the strange particles that are produced in these high energy
935 collisions is through jets, which are sprays of hadrons that come from a hard inter-
936 action of the partons inside the nuclei. By looking at how a high-momentum hadron
937 (that represents a jet direction) and a lower momentum strange hadron are aligned
938 in azimuthal angle, it is possible to separate the processes that create strangeness
939 between hard (jet-related) and soft (QGP-related) ones. This angular correlation
940 method can be used to further the understanding of how strangeness production de-

941 pends on the multiplicity in these different regimes, thus providing insight to the
942 onset of strangeness enhancement in smaller collision systems.

943 This thesis presents the first results using angular correlations to measure jet and
944 non-jet Λ and charged hadron production in p–Pb collisions at $\sqrt{s_{\text{NN}}} = 5.02$ TeV. By
945 using the technique of two-particle angular correlations, the production of Λ baryons
946 can be separated into different kinematic regions: the near-side region (associated
947 with jet-like strangeness production without QGP modification) away-side region
948 (associated with jet-like production in the presence of the QGP), and the underlying
949 event (tied to the uncorrelated strangeness production in the QGP). Both the yields
950 and the jet widths on the near- and away-side regions are extracted from the azimuthal
951 correlation functions and studied as a function of associated momentum and event
952 multiplicity. A strong dependence on multiplicity is observed for both the near-
953 and away-side yields in the case of the Λ , whereas the charged hadron associated
954 yields exhibit a much smaller (nearly statistically insignificant) dependence. The
955 away-side yields also show a systematically larger increase with multiplicity than the
956 near-side yields for both cases, hinting at modification of the away-side production
957 due to jet-QGP interactions. The h- Λ and h-h near-side jet widths reveal a large
958 dependence on p_{T} , becoming more collimated as momentum increases. The widths of
959 the away-side jets are found to be independent of both p_{T} and multiplicity, however
960 the larger systematic uncertainties introduce difficulties with excluding flat behavior.
961 Comparing width values of the h- Λ and h-h correlations, the h- Λ near-side widths
962 are found to be significantly ($> 2\sigma$) larger than the dihadron widths, whereas the
963 away-side widths are consistent within uncertainties. This indicates that Λ baryons
964 are more readily produced in the peripheral regions of the jet cone, whereas charged
965 hadrons are produced closer to the jet axis. This hints at a modification of the jet
966 fragmentation process for strange hadrons, as more massive particles (like the Λ) are
967 expected to be produced closer to the jet axis.

968 The yield ratios $R_i^{\Lambda/h}$ and $R_i^{\Lambda/\phi}$ ($i = \text{near-side jet, away-side jet, UE}$) are also
969 studied as a function of associated p_{T} and multiplicity. The Λ/h ratios exhibit a clear
970 ordering in each region for the entire multiplicity range in both p_{T} bins, with the
971 UE ratios being larger than the away-side ratios, which are larger than the near-side
972 ratios. This indicates that relative Λ production is larger in the UE (QGP) when
973 compared to the jet-like regions. The Λ/h ratios in each region also reveal a strong
974 dependence on multiplicity, with slopes that are greater than zero by nearly 5σ for

975 both momentum bins. This indicates that while the overall Λ production is mostly
976 concentrated in the UE, the observed enhancement of Λ production with increasing
977 multiplicity is *also* driven by the jet-like regions. Furthermore, the away-side slopes
978 are found to be systematically higher than the near-side slopes, indicating that the
979 away-side Λ production is more strongly enhanced than the near-side Λ production
980 with increasing multiplicity. Again, this suggests that the away-side jet strangeness
981 production is modified by medium interactions. The Λ/ϕ ratios in the near-side jet
982 region are measured to be systematically higher than both the away-side and UE
983 ratios, hinting at a suppression of ϕ mesons along the jet axis due to the lack of
984 available s -quarks in the unmodified jet. The slopes of these ratios in all kinematic
985 regions are consistent with zero, indicating that the ratio is independent of collision
986 centrality.

987 The measurements in this thesis are compared with theoretical predictions from
988 the PHSD, EPOS and DPMJET models. PHSD is found to be in good agreement with
989 all dihadron measurements, but fails to describe the overall Λ yields. This is likely
990 due to the requirement of a high momentum trigger hadron, which are not readily
991 produced within the model. Even still, the shape of the near-side peak in the h- Λ
992 correlation distribution is well-described by PHSD. EPOS, on the otherhand, is able
993 to describe the Λ and hadron yields very well, but the correlation distributions are
994 dominated by elliptic flow, making it impossible to extract the jet-like components.
995 This flow contribution is much larger for the h- Λ distributions, indicating that Λ
996 baryons in EPOS are mostly produced within the hydronamic core. The predicted
997 near- and away-side yields from DPMJET are found to be in relatively good agreement
998 with data in the dihadron case, but the h- Λ yield predictions deviate from data by a
999 large ($> 40\%$) margin. DPMJET also fails to predict any of the observed multiplicity
1000 dependence for both the h- Λ and h-h jet yields. However, the model is able to closely
1001 predict the near-side widths of the dihadron distributions across all multiplicity and
1002 momentum ranges, although it underpredicts both the h- Λ near-side widths and
1003 the away-side widths for both (Λ , h) cases. The model also predicts a difference
1004 between the h- Λ and h-h near-side widths, which is observed in data as well. This
1005 indicates that whatever process responsible for the production of strangeness in the
1006 periphery of the jet cone is contained within DPMJET. The per-trigger Λ/h and Λ/ϕ
1007 yield ratios are consistently underpredicted by DPMJET, and exhibit no multiplicity
1008 dependence. Even still, DPMJET manages to predict the ordering of the Λ/h ratios

1009 in each region (UE > away-side jet > near-side jet) and the enhancement of the
1010 jet-like Λ/ϕ ratio when compared to the UE region. Thus the softer, uncorrelated
1011 processes implemented in DPMJET are responsible for the majority of the relative
1012 strangeness production.

1013 **2.1 Future outlook**

1014 The measurements presented in this thesis strongly indicate that, while the dom-
1015 inating component for strangeness production comes from the QGP, the observed
1016 *enhancement* of this production as a function of multiplicity has a large contribution
1017 from the jet-like regions. More still, the away-side jet component appears to undergo
1018 a larger enhancement than the near-side, hinting that the jet and medium are inter-
1019 acting in such a way that strangeness is more readily produced. These observations
1020 can be used to help fuel the theoretical models used to describe particle collisions, as
1021 such models are currently incapable of describing these results in their entirety.

1022 The techniques presented in this thesis can be easily extended to other collision
1023 systems, such as pp and Pb–Pb collisions, along with other particle species, such as
1024 the K^0 . With the advent of the Run 3 data-taking period at the LHC, the ALICE
1025 detector will be able to collect more data than ever before, allowing for more precise
1026 measurements of these observables across a wider range of particles and collision
1027 systems. Such measurements will help further constrain the microscopic origins of
1028 this strange enhancement, thus providing more insight into the nature of the QGP
1029 and the universe as a whole.

1030 **Appendix A: Resonance technique for Λ**
1031 **reconstruction**

1032 **A.1 Introduction**

1033 This portion of the appendix is dedicated to describing the analysis procedure for
1034 generating the $h\text{-}\Lambda$ correlation distributions using lambdas which are reconstructed
1035 using the **resonance technique**, where all proton-pion pairs in an event are com-
1036 bined to form Λ candidates. All of the proton and pion daughter tracks meet the
1037 same selection criteria as the tracks used in the V^0 technique, described in Table ??.
1038 All in all, the procedure is very similar to the one described in Chapter ??, but with
1039 a few key differences that will be highlighted in the following sections.

1040 **A.2 Combinatorial background estimation**

1041 As Λ baryons reconstructed using the resonance technique will have a much larger
1042 combinatorial background than those from the nominal procedure, the final correla-
1043 tion will contain a higher fraction of $h\text{-}(p\pi)$ pairs that need to be removed. While
1044 the sideband subtraction technique provides a general procedure for removing these
1045 pairs, the signal S and the background B of the Λ invariant mass distribution must be
1046 well described. To estimate these quantities, the following techniques were explored:

- 1047 • **Like-sign $p\pi$ pairs** - Reconstruct the invariant mass of like-sign (LS) $p\pi$ pairs,
1048 and scale the like-sign $p\pi$ distribution to the unlike-sign (US) $p\pi$ distribution
1049 in a region outside of the Λ signal region.
- 1050 • **Rotated $p\pi$ pairs** - Reconstruct the invariant mass of US $p\pi$ pairs, but rotate
1051 either the pion or proton around the z-axis by π radians, and scale the rotated
1052 $p\pi$ distribution to the original US sign $p\pi$ distribution in a region outside of
1053 the Λ signal region.

- 1054 • **Voigtian + polynomial fit** - Perform a standard fitting procedure using a
 1055 Voigtian distribution for the signal along with a second-order polynomial for
 1056 the background.

1057 The last technique will be addressed first, as it fails to properly estimate the signal
 1058 and background in data. To illustrate this, the best possible fits in data are found
 1059 and the corresponding signal shape is extracted and compared with the signal shape
 1060 in Monte Carlo using full track reconstruction via GEANT. This comparison is done
 1061 for the 20-50% multiplicity bin in Figure A.1. Note that the background shown in the
 1062 MC plot is the true combinatorial background, as the $p\pi$ pairs are accessed directly
 1063 at the generator level to confirm they did not come from a Λ decay.

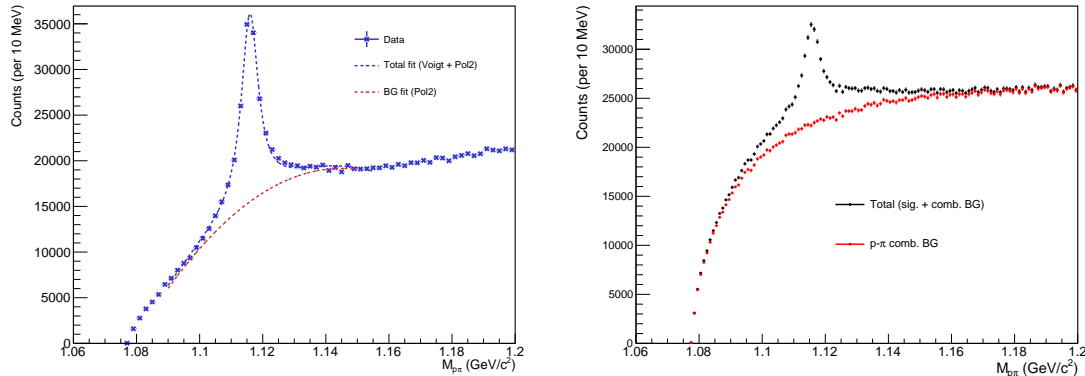


Figure A.1: Left: Invariant mass distribution with corresponding Voigt + Polynomial fit in the 20-50% multiplicity bin (data). Right: The signal and background shapes in MonteCarlo (MC). Note that even though MC appears to have a completely different S/B, the signal shapes should be similar. The fit in data appears to be massively underestimating the Λ signal, as the MC sample indicates there is Λ signal where the total data fit converges with the BG fit.

1064 This plot shows the main issue with reconstructing Λ baryons using the resonance
 1065 technique: the tails of the signal distribution are much wider than the signal distri-
 1066 bution obtained using the V^0 method. This is due to the fact that the kinematics
 1067 of the corresponding daughter tracks are calculated assuming they originated from
 1068 the primary vertex, which is only approximately true in the cases where the Λ is
 1069 short-lived. This is different than the V^0 method, which calculates the kinematics for
 1070 the daughter tracks assuming they originated from the secondary vertex. The wider
 1071 tails of the distribution make it extremely difficult to describe using any common

1072 distribution, thus all techniques that rely on fitting the signal shape are not viable.
 1073 Because of this, only the first two techniques (like-sign and rotated p π pairs) will be
 1074 considered for the rest of this analysis.

1075 To determine which of the two remaining techniques is more effective, the back-
 1076 ground shape of the Λ invariant mass distribution for both techniques in MonteCarlo
 1077 is compared to the ground-truth background shape. The resulting invariant mass
 1078 distributions from like-sign and rotated p π pairs are shown in Figure A.2, along with
 1079 a comparison of the extracted signal shapes. The LS and rotated p π distributions are
 1080 scaled to match the US distribution in the sideband region, which will be discussed
 1081 in the next section. The LS p π pairs match the background shape of the Λ invariant
 1082 mass distribution more closely than the rotated p π pairs, so they are used to estimate
 1083 the combinatorial background in the Λ invariant mass distribution in data.

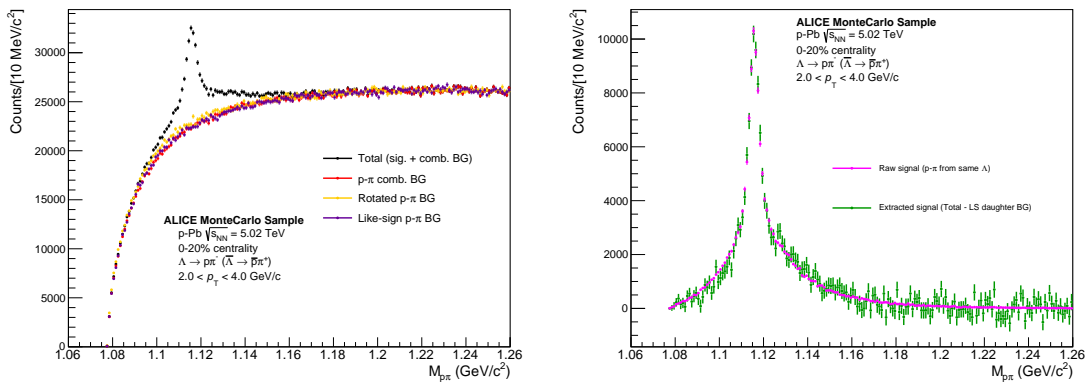


Figure A.2: Left: Invariant mass distribution for reconstructed unlike-sign p π pairs (black) in the MonteCarlo sample. The like-sign p π pair mass distribution (purple) and unlike-sign rotated p π distributions are scaled to match the unlike-sign distribution outside of the Λ signal range. The true combinatorial background (red) matches most closely with the like-sign pairs. Right: The actual Λ signal (magenta) compared with the result of subtracting the like-sign from the total unlike-sign p π distribution (green). The two distributions show good agreement.

1084 A.3 Signal and sideband regions

1085 As the invariant mass distributions from lambdas reconstructed using the resonance
 1086 technique are very different from those reconstructed using the V⁰ technique, so

too must the signal and sideband regions be different. The signal region was again chosen to maximize significance across all multiplicity bins, and is defined as the range $1.014 < M_{p\pi} < 1.026 \text{ GeV}/c^2$. Choosing the sideband region is a more complicated procedure, as there is no obvious region in the invariant mass distribution where the signal vanishes. Instead, the sideband region is chosen to minimize the difference between the extracted signal in data and the signal shape in MonteCarlo, which can be seen in Figure A.3. The resulting sideband region is $1.160 < M_{p\pi} < 1.180 \text{ GeV}/c^2$.

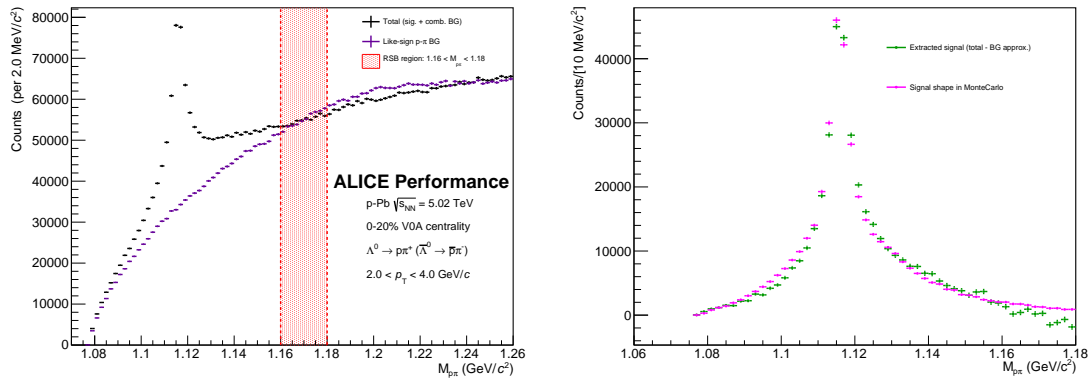


Figure A.3: Left: Invariant Mass distribution for unlike-sign $p\pi$ pairs (black) along with the like-sign $p\pi$ background (purple) and the sideband region (red) in the 0-20% multiplicity bin. Right: The extracted signal (green) compared with the resonance-technique reconstructed signal shape in MonteCarlo (magenta). The sideband region was chosen to minimize the differences between these distributions.

1094 A.3.1 Efficiency correction

1095 Again, the resonance technique-based Λ reconstruction efficiency is calculated in a
1096 similar manner as the V^0 technique, using the formula

$$\epsilon(x_1, x_2, \dots, x_n) = \frac{N_{\text{reco.}}(x_1, x_2, \dots, x_n)}{N_{\text{gen.}}(x_1, x_2, \dots, x_n)}, \quad (\text{A.1})$$

1097 where $N_{\text{reco.}}$ and $N_{\text{gen.}}$ are the reconstructed and generated particle distributions with
1098 kinematic variables x_1, x_2, \dots, x_n . The main difference from the V^0 efficiency computa-
1099 tion comes from $N_{\text{reco.}}$, where each Λ candidate is generated using the following
1100 procedure:

- 1101 • Find all protons and pions within the track list that pass the daughter selection
1102 criteria

- 1103 • For each proton in the list, determine if it came from a Λ (at generator level)
- 1104 • If the proton came from a Λ , loop through the pion list until the pion that came
1105 from the same Λ is found (again, verified at the generator level)
- 1106 • Reconstruct the Λ using the daughter tracks found in the previous two steps
- 1107 • Only keep the Λ if $|\eta| < 0.8$
- 1108 The denominator $N_{\text{gen.}}$ is calculated in the same way as the V^0 technique. The
1109 resulting efficiency is shown as a function of p_T for each multiplicity bin in Figure A.4.
1110 As expected, the efficiency is higher than the V^0 technique, as every Λ reconstructed
1111 using the resonance technique would also be reconstructed using the V^0 technique.

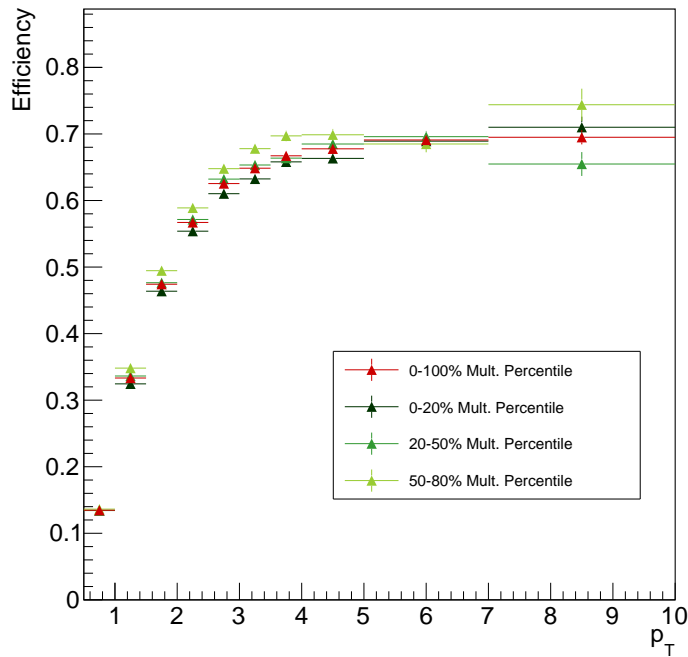


Figure A.4: Efficiency vs. p_T for Λ reconstruction using resonance technique for each multiplicity bin, along with an integrated 0-100% point in red. There does not appear to be any significant dependence on multiplicity. Also worth nothing that the efficiency is higher for this technique when compared to the V^0 technique, as expected (all AOD tracks from V^0 finder daughters are also in total AOD track list).

1112 **A.4 Corrections to the h- Λ distributions**

1113 All of the efficiency and acceptance corrections are applied to the resonance technique-based h- Λ distribution in the same way as the V⁰ technique. The only difference comes
1114 from the removal of the combinatorial background, as:

- 1116 1. The signal S and background B are calculated in a slightly different manner,
1117 and
- 1118 2. The sideband region is vastly different.

1119 For the first point, the signal and background are calculated via bin-wise summation
1120 of the invariant mass distribution using the LS p π pairs as an estimate for the
1121 background, scaled to the US distribution in the sideband region.

1122 The second point is mostly inconsequential as the h-p π distributions are very
1123 similar in a wide range of sideband regions, as shown in Figure A.5. The nominal
1124 sideband region was chosen to be $1.160 < M_{\text{SSB}} < 1.180 \text{ GeV}/c^2$, but any region with
1125 a lower bound greater than $1.160 \text{ GeV}/c^2$ and upper bound less than $1.22 \text{ GeV}/c^2$
1126 should produce similar results.

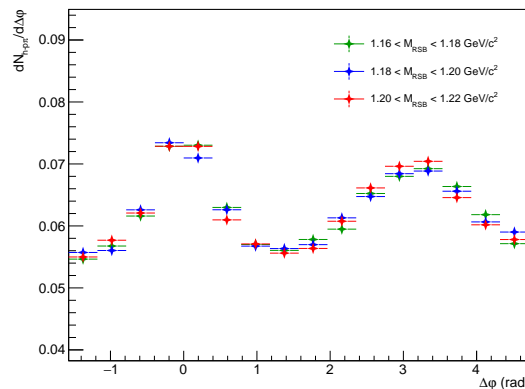


Figure A.5: The projected $\Delta\varphi$ distributions for different choices of sideband, taken within the $-1.2 < \Delta\eta < 1.2$ region. The correlation shapes are identical within the statistical errors.

1127 The signal scaling factor is calculated in the same way as it is in Equation ??, but
1128 with the residual now generated by subtracting the sideband-scaled LS p π pairs from
1129 the US distribution. The two-track efficiency correction is not applied, as the tools

1130 used to calculate the $\epsilon_{\text{pair}}(\Delta\varphi, \Delta\eta)$ template were not developed before the resonance
 1131 technique-based analysis was completed.

1132 A.5 MC closure test

1133 An MC closure test was also performed for the resonance technique-based analysis,
 1134 and the results are shown in Figure A.6. The ratio is consistent with unity, but the
 1135 statistical fluctuations make it difficult to draw any meaningful conclusions.

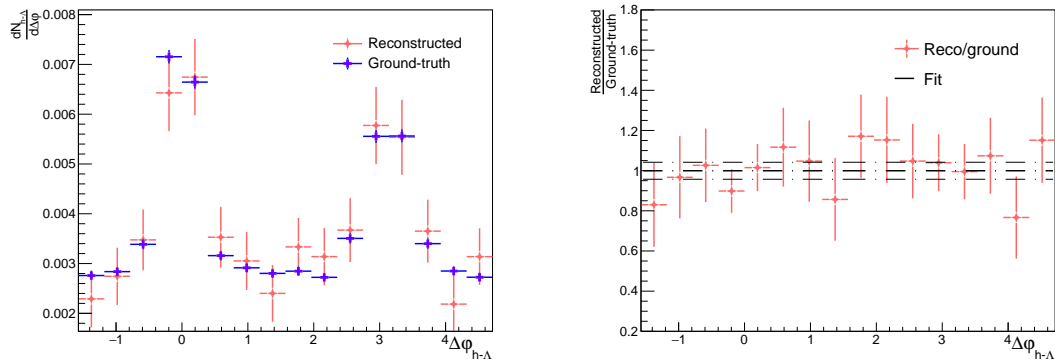


Figure A.6: The reconstructed (red) and ground-truth (blue) $h\text{-}\Lambda_{\text{res}}$ $\Delta\varphi$ distributions along with a (reconstructed)/(ground-truth) ratio and straight-line fit. The fit is technically consistent with unity, but the statistical fluctuations are quite large.

1136 As the reconstructed distribution has not been corrected for the two-track merging
 1137 effect, it is surprising that the ratio does not exhibit a significant deviation from unity
 1138 at small $\Delta\varphi$. This is likely due to two factors:

- 1139 1. The resonance technique has a much lower S/B, and therefore the sideband
 1140 subtraction introduces a large amount of statistical fluctuations making such
 1141 deviations difficult to observe, and
- 1142 2. The reconstructed daughter tracks have a larger fraction of higher quality tracks
 1143 when compared to the V^0 technique, and those tracks are less likely to be merged
 1144 over by the trigger during reconstruction.

1145 To elaborate on the second point, while the resonance and V^0 techniques use the
 1146 same loose quality cuts, the daughter tracks coming from the V^0 technique must

1147 have a resolvable secondary vertex, which biases the corresponding Λ sample to those
 1148 with a higher decay length. As discussed in ??, the two-track merging effect is
 1149 more pronounced at larger decay lengths, thus the $h\text{-}\Lambda$ distributions using the V^0
 1150 reconstruction technique will have a larger fraction of merged tracks when compared
 1151 to the resonance technique-based distributions.

1152 To further investigate this surprising closure of the resonance technique-based $h\text{-}\Lambda$
 1153 $\Delta\varphi$ distributions, the same closure test is performed, but for the reconstructed $h\text{-}\Lambda$
 1154 distribution, the Λ candidate is required to have have a corresponding particle at the
 1155 generator-level, making the combinatorial background exactly zero and removing the
 1156 need for sideband subtraction. The results of this test are shown in Figure A.7. The
 1157 ratio is no longer consistent with unity at small $\Delta\varphi$, as expected¹

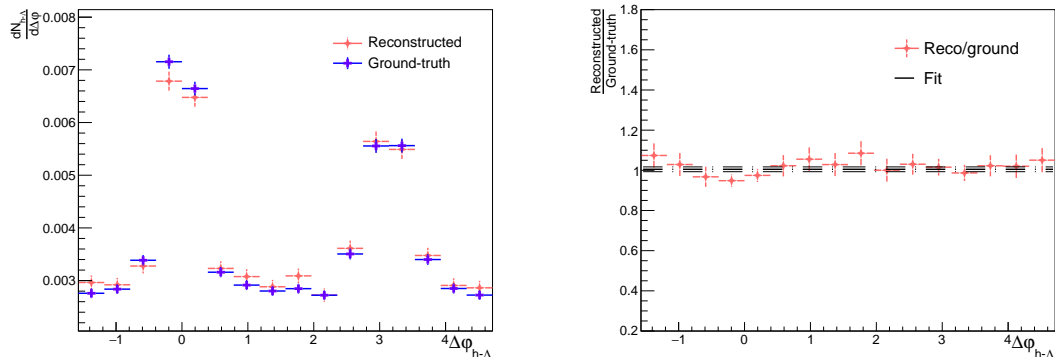


Figure A.7: The reconstructed (red) and ground-truth (blue) $h\text{-}\Lambda_{\text{res}}$ $\Delta\varphi$ distributions along with a (reconstructed)/(ground-truth) ratio and straight-line fit, but instead requiring the reconstructed Λ to have a corresponding particle at the generator level to make sideband subtraction unnecessary. The result is no longer consistent with unity at small $\Delta\varphi$ due to the track merging effect, but the non-closure is much smaller than the V^0 technique.

1158 A.6 Some additional results

1159 A comparison of the final per-trigger $h\text{-}\Lambda$ $\Delta\varphi$ correlation structure from the resonance
 1160 and V^0 -based techniques was shown in Chapter ??, but it can be seen again in

¹It is strange to *want* non-closure, but it would be even stranger if the track merging effect were somehow not present in the resonance technique-based analysis.

1161 Figure A.8. As mentioned previously, the correlation shapes are nearly identical, with
 1162 the resonance technique having slightly larger uncertainties due to the combinatorial
 1163 background subtraction.

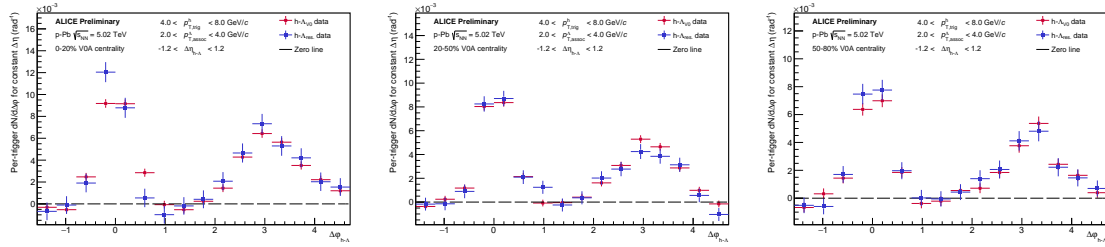


Figure A.8: The final per-trigger $h\Lambda \Delta\varphi$ correlations for Λ s reconstructed using the resonance technique (blue) and the V^0 -based technique (red) in the 0-20% (left), 20-50% (middle) and 50-80% (right) multiplicity bins, taken in the associated momentum range $2.0 < p_T < 4.0 \text{ GeV}/c$, after the subtraction of the UE. The distributions show good agreement across all multiplicity bins, indicating that the V^0 -based reconstruction technique is not introducing a bias in the correlation shape.

1164 Additionally, the per-trigger near- and away-side pairwise yields and the $(h\Lambda)/(h-h)$
 1165 ratios with Λ s reconstructed using the resonance technique are shown in Figure A.9.
 1166 The results are qualitatively very similar to the nominal results, indicating that the
 1167 resonance technique is a reasonably viable alternative to the V^0 technique. How-
 1168 ever, due to the larger combinatorial background (and likely very large systematic
 1169 uncertainties), the V^0 technique is still the preferred method for Λ reconstruction.

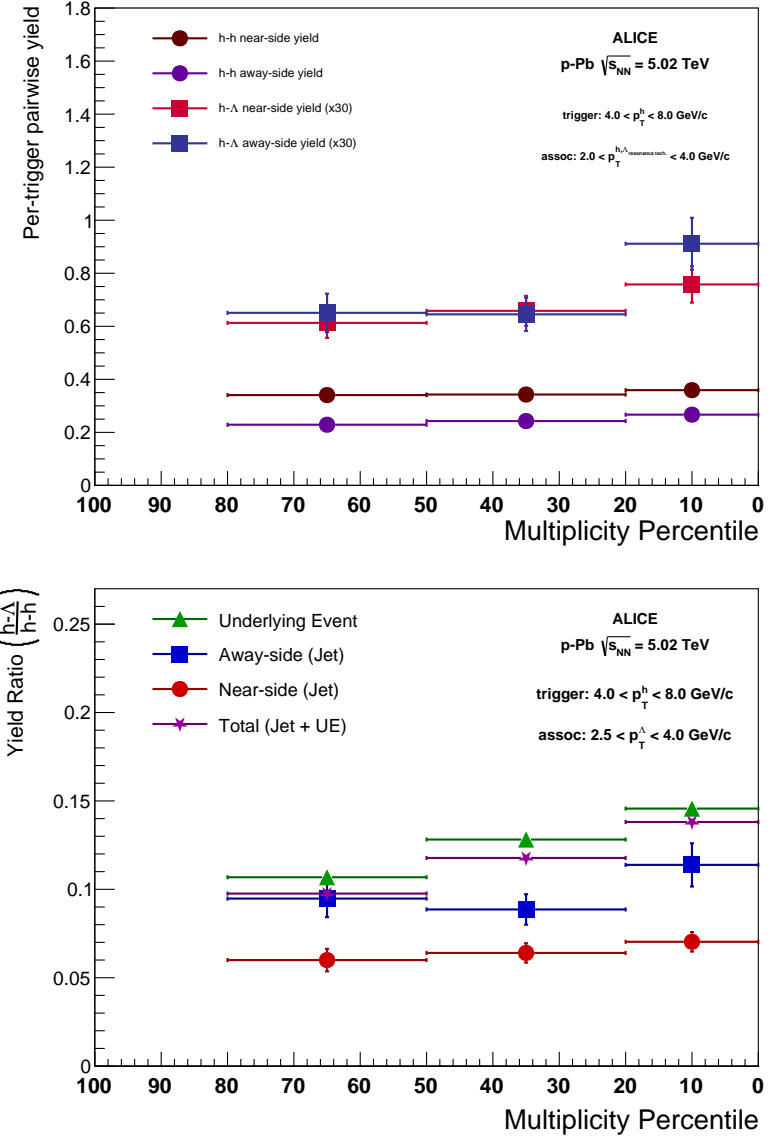


Figure A.9: The final $h-\Lambda$ and $h-h$ per-trigger pairwise jet yields (top) and $(h-\Lambda)/(h-h)$ yield ratios (bottom) vs. multiplicity in the associated momentum range $2.0 < p_T < 4.0 \text{ GeV}/c$ for Λ s reconstructed using the resonance technique. The general trends are similar to the nominal V^0 technique-based procedure, with larger statistical uncertainties.

Bibliography

- 1171 [1] B. Pullman, *The Atom in the History of Human Thought*. Oxford: Oxford
1172 University Press, 1998, ISBN: 978-0-19-515040-7 (cit. on p. 2).
- 1173 [2] J. Dalton, “Experimental enquiry into the proportion of the several gases
1174 or elastic fluids, constituting the atmosphere,” *Memoirs of the Literary and*
1175 *Philosophical Society of Manchester*, vol. 1, pp. 244–258, 1805 (cit. on p. 2).
- 1176 [3] E. R. Scerri, *The Periodic Table: A Very Short Introduction*. Oxford University
1177 Press, Jul. 2019, pp. 117–123, ISBN: 9780198842323. DOI: 10.1093/actrade/
1178 9780198842323.001.0001. [Online]. Available: <https://doi.org/10.1093/actrade/9780198842323.001.0001> (cit. on p. 2).
- 1180 [4] D. Mendeleev, “The natural system of elements and its application to the
1181 indication of the properties of undiscovered elements,” *Journal of the Russian*
1182 *Chemical Society*, vol. 3, pp. 25–56, 1871 (cit. on p. 2).
- 1183 [5] I. Falconer, “J J Thomson and the discovery of the electron,” *Physics Educa-*
1184 *tion*, vol. 32, no. 4, p. 226, 1997. DOI: 10.1088/0031-9120/32/4/015.
1185 [Online]. Available: <https://dx.doi.org/10.1088/0031-9120/32/4/015>
1186 (cit. on p. 3).
- 1187 [6] E. Rutherford, “The scattering of α and β particles by matter and the structure
1188 of the atom,” *Philosophical Magazine Series 6*, vol. 21, pp. 669–688, 1911 (cit.
1189 on p. 3).
- 1190 [7] J. Chadwick, “Possible existence of a neutron,” *Nature*, vol. 129, p. 312, 1932
1191 (cit. on p. 3).
- 1192 [8] C. D. Anderson, “The apparent existence of easily deflectable positives,” *Sci-*
1193 *ence*, vol. 76, no. 1967, pp. 238–239, 1932. DOI: 10.1126/science.76.1967.
1194 238. eprint: <https://www.science.org/doi/pdf/10.1126/science.76.1967.238>. [Online]. Available: <https://www.science.org/doi/abs/10.1126/science.76.1967.238> (cit. on p. 3).

- 1197 [9] S. H. Neddermeyer and C. D. Anderson, “Note on the nature of cosmic-ray
1198 particles,” *Phys. Rev.*, vol. 51, pp. 884–886, 10 1937. DOI: 10.1103/PhysRev.
1199 51.884. [Online]. Available: <https://link.aps.org/doi/10.1103/PhysRev.51.884> (cit. on p. 3).
- 1200
- 1201 [10] R. Brown *et al.*, “Observations with Electron-Sensitive Plates Exposed to
1202 Cosmic Radiation,” *Nature*, vol. 163, no. 4133, pp. 82–87, Jan. 1949. DOI:
1203 10.1038/163082a0 (cit. on p. 3).
- 1204
- 1205 [11] V. D. Hopper and S. Biswas, “Evidence concerning the existence of the new
1206 unstable elementary neutral particle,” *Phys. Rev.*, vol. 80, pp. 1099–1100, 6
1207 1950. DOI: 10.1103/PhysRev.80.1099. [Online]. Available: <https://link.aps.org/doi/10.1103/PhysRev.80.1099> (cit. on p. 3).
- 1208
- 1209 [12] A. Barbaro-Galtieri *et al.*, “Apparent violation of the $\Delta S = \Delta Q$ rule by lep-
1210 tonic Σ^+ decay,” *Phys. Rev. Lett.*, vol. 9, pp. 26–29, 1 1962. DOI: 10.1103/
1211 PhysRevLett.9.26. [Online]. Available: <https://link.aps.org/doi/10.1103/PhysRevLett.9.26> (cit. on p. 3).
- 1212
- 1213 [13] T. Nakano and K. Nishijima, “Charge Independence for V-particles,” *Progress
of Theoretical Physics*, vol. 10, no. 5, pp. 581–582, 1953. DOI: 10.1143/PTP.
1214 10.581 (cit. on p. 3).
- 1215
- 1216 [14] R. Serway, C. Moses, and C. Moyer, *Modern Physics*. Cengage Learning, 2004,
1217 pp. 12–13, ISBN: 9780534493394. [Online]. Available: <https://books.google.com/books?id=Yfo3rnt3bkEC> (cit. on p. 3).
- 1218
- 1219 [15] M. Gell-Mann, “The Eightfold Way: A theory of strong interaction symmetry,”
1220 Mar. 1961. DOI: 10.2172/4008239. [Online]. Available: <https://www.osti.gov/biblio/4008239> (cit. on pp. 3, 4, 11).
- 1221
- 1222 [16] Y. Ne’eman, “Derivation of strong interactions from a gauge invariance,” *Nu-
1223 clear Physics*, vol. 26, no. 2, pp. 222–229, 1961. DOI: 10.1016/0029-5582(61)
1224 90134-1 (cit. on p. 3).
- 1225
- 1226 [17] W. Heisenberg, “Über den Bau der Atomkerne. I,” *Zeitschrift fur Physik*,
vol. 77, no. 1-2, pp. 1–11, Jan. 1932. DOI: 10.1007/BF01342433 (cit. on
p. 3).

- 1227 [18] M. Gell-Mann, “Isotopic Spin and New Unstable Particles,” *Physical Review*,
1228 vol. 92, no. 3, pp. 833–834, Nov. 1953. DOI: 10.1103/PhysRev.92.833 (cit. on
1229 pp. 3, 23, 24, 31).
- 1230 [19] T. Nakano and K. Nishijima, “Charge Independence for V-particles,” *Progress*
1231 *of Theoretical Physics*, vol. 10, no. 5, pp. 581–582, Nov. 1953. DOI: 10.1143/
1232 PTP.10.581 (cit. on p. 4).
- 1233 [20] M. Gell-Mann, “The interpretation of the new particles as displaced charge
1234 multiplets,” *Il Nuovo Cimento*, vol. 4, no. S2, pp. 848–866, Apr. 1956. DOI:
1235 10.1007/BF02748000 (cit. on p. 4).
- 1236 [21] M. Gell-Mann, “A schematic model of baryons and mesons,” *Physics Letters*,
1237 vol. 8, no. 3, pp. 214–215, Feb. 1964. DOI: 10.1016/S0031-9163(64)92001-3
1238 (cit. on p. 4).
- 1239 [22] A. Pickering, *Constructing quarks*. University of Chicago Press, 1999, pp. 114–
1240 125. DOI: 10.7208/chicago/9780226667997.003.0007 (cit. on p. 5).
- 1241 [23] B. J. Bjørken and S. L. Glashow, “Elementary particles and SU(4),” *Physics*
1242 *Letters*, vol. 11, no. 3, pp. 255–257, Aug. 1964. DOI: 10.1016/0031-9163(64)
1243 90433-0 (cit. on p. 5).
- 1244 [24] S. Glashow, “The hunting of the atoms and their nuclei: Protons and neu-
1245 trons,” *New York Times*, Jul. 1976. [Online]. Available: <https://www.nytimes.com/1976/07/18/archives/the-hunting-of-the-atoms-and-their-nuclei-protons-and-neutrons.html> (cit. on p. 5).
- 1246 [25] S. L. Glashow, J. Iliopoulos, and L. Maiani, “Weak Interactions with Lepton-
1247 Hadron Symmetry,” *Phys Rev D*, vol. 2, no. 7, pp. 1285–1292, Oct. 1970. DOI:
1248 10.1103/PhysRevD.2.1285 (cit. on p. 5).
- 1249 [26] H. Kendall, *Deep inelastic scattering: Experiments on the proton and the ob-
1250 servation of scaling*, 1990. [Online]. Available: <https://www.nobelprize.org/uploads/2018/06/kendall-lecture.pdf> (visited on 08/21/2023) (cit.
1251 on pp. 5, 6).
- 1252 [27] J. Friedman, *Deep inelastic scattering: Comparisons with the quark model*,
1253 1990. [Online]. Available: <https://www.nobelprize.org/uploads/2018/06/friedman-lecture.pdf> (visited on 08/21/2023) (cit. on p. 5).

- 1258 [28] R. Taylor, *Deep inelastic scattering: The early years*, 1990. [Online]. Available:
1259 <https://www.nobelprize.org/uploads/2018/06/taylor-lecture.pdf>
1260 (visited on 08/21/2023) (cit. on p. 5).
- 1261 [29] E. D. Bloom *et al.*, “High-Energy Inelastic e-p Scattering at 6° and 10° ,”
1262 *Physical Review Letters*, vol. 23, no. 16, pp. 930–934, Oct. 1969. DOI: 10.1103/PhysRevLett.23.930 (cit. on p. 5).
- 1264 [30] E. D. Bloom *et al.*, “High-Energy Inelastic e-p Scattering at 6° and 10° ,”
1265 *Physical Review Letters*, vol. 23, no. 16, pp. 930–934, Oct. 1969. DOI: 10.1103/PhysRevLett.23.930 (cit. on p. 5).
- 1267 [31] J. Bjorken, “Current algebra at small distances,” Jun. 2018. [Online]. Available: <https://www.osti.gov/biblio/1444446> (cit. on p. 6).
- 1269 [32] R. P. Feynman, “The behavior of hadron collisions at the uncertainties from
1270 these sources exhibit no multiplicity dependence, and a very small depen-
1271 dence on p_T . extreme energies,” in *Special Relativity and Quantum Theory: A Collection of Papers on the Poincaré Group*, M. E. Noz and Y. S. Kim,
1272 Eds. Dordrecht: Springer Netherlands, 1988, pp. 289–304, ISBN: 978-94-009-
1273 3051-3. DOI: 10.1007/978-94-009-3051-3_25. [Online]. Available: https://doi.org/10.1007/978-94-009-3051-3_25 (cit. on p. 6).
- 1276 [33] J. Aubert *et al.*, “Experimental observation of a heavy particle J ,” *Physical
1277 Review Letters*, vol. 33, Dec. 1974 (cit. on p. 6).
- 1278 [34] H. Fritzsch, M. Gell-Mann, and H. Leutwyler, “Advantages of the color octet
1279 gluon picture,” *Physics Letters B*, vol. 47, no. 4, pp. 365–368, Nov. 1973. DOI:
1280 10.1016/0370-2693(73)90625-4 (cit. on p. 7).
- 1281 [35] D. J. Gross and F. Wilczek, “Ultraviolet Behavior of Non-Abelian Gauge The-
1282 ories,” *Physical Review Letters*, vol. 30, no. 26, pp. 1343–1346, Jun. 1973. DOI:
1283 10.1103/PhysRevLett.30.1343 (cit. on p. 7).
- 1284 [36] H. D. Politzer, “Reliable Perturbative Results for Strong Interactions?” *Phys-
1285 ical Review Letters*, vol. 30, no. 26, pp. 1346–1349, Jun. 1973. DOI: 10.1103/
1286 PhysRevLett.30.1346 (cit. on p. 7).
- 1287 [37] P. Söding, *Twenty-five years of gluons*, 2004. [Online]. Available: <https://cerncourier.com/a/twenty-five-years-of-gluons/> (cit. on pp. 7, 14).

- 1289 [38] P. Söding, “On the discovery of the gluon,” *European Physical Journal H*,
1290 vol. 35, no. 1, pp. 3–28, Jul. 2010. DOI: 10.1140/epjh/e2010-00002-5 (cit.
1291 on p. 7).
- 1292 [39] A. Salam and J. C. Ward, “Weak and electromagnetic interactions,” *Il Nuovo
Cimento*, vol. 11, no. 4, pp. 568–577, Feb. 1959. DOI: 10.1007/BF02726525
1294 (cit. on p. 7).
- 1295 [40] S. Weinberg, “A Model of Leptons,” *Physical Review Letters*, vol. 19, no. 21,
1296 pp. 1264–1266, Nov. 1967. DOI: 10.1103/PhysRevLett.19.1264 (cit. on p. 7).
- 1297 [41] P. W. Higgs, “Broken symmetries and the masses of gauge bosons,” *Phys. Rev.
Lett.*, vol. 13, pp. 508–509, 16 1964. DOI: 10.1103/PhysRevLett.13.508.
1299 [Online]. Available: <https://link.aps.org/doi/10.1103/PhysRevLett.13.508> (cit. on pp. 7–9).
- 1300 [42] P. T. Smith, “Reporting New Evidence of Gravitons,” in *14th International
Symposium on Nuclei in the Cosmos (NIC2016)*, S. Kubono *et al.*, Eds., Jan.
1303 2017, 020101, p. 020101. DOI: 10.7566/JPSCP.14.020101 (cit. on p. 7).
- 1304 [43] G. Jungman, M. Kamionkowski, and K. Griest, “Supersymmetric dark mat-
1305 ter,” *Physics Reports*, vol. 267, no. 5, pp. 195–373, 1996, ISSN: 0370-1573.
1306 DOI: [https://doi.org/10.1016/0370-1573\(95\)00058-5](https://doi.org/10.1016/0370-1573(95)00058-5). [Online].
1307 Available: <https://www.sciencedirect.com/science/article/pii/0370157395000585> (cit. on p. 7).
- 1308 [44] G. Esposito, *An introduction to quantum gravity*, 2011. arXiv: 1108.3269
[hep-th] (cit. on p. 8).
- 1311 [45] G. Aad *et al.*, “Observation of a new particle in the search for the Standard
1312 Model Higgs boson with the ATLAS detector at the LHC,” *Phys. Lett. B*,
1313 vol. 716, pp. 1–29, 2012. DOI: 10.1016/j.physletb.2012.08.020. arXiv:
1314 1207.7214 [hep-ex] (cit. on p. 9).
- 1315 [46] S. Chatrchyan *et al.*, “Observation of a New Boson at a Mass of 125 GeV
1316 with the CMS Experiment at the LHC,” *Phys. Lett. B*, vol. 716, pp. 30–61,
1317 2012. DOI: 10.1016/j.physletb.2012.08.021. arXiv: 1207.7235 [hep-ex]
1318 (cit. on p. 9).

- 1319 [47] R. Shivni, *The deconstructed standard model equation*, Sep. 2023. [Online].
1320 Available: [https://www.symmetrymagazine.org/article/the-deconstructed-](https://www.symmetrymagazine.org/article/the-deconstructed-standard-model-equation?language_content_entity=und)
1321 [standard-model-equation?language_content_entity=und](#) (cit. on p. 10).
- 1322 [48] F. Gross *et al.*, “50 Years of Quantum Chromodynamics,” Dec. 2022. arXiv:
1323 2212.11107 [hep-ph] (cit. on pp. 10, 11).
- 1324 [49] Wikipedia, *Structure constants — Wikipedia, the free encyclopedia*, <http://en.wikipedia.org/w/index.php?title=Structure%20constants&oldid=1160301276>, [Online; accessed 07-October-2023], 2023 (cit. on p. 11).
- 1327 [50] K. Chetyrkin and A. Rétey, “Renormalization and running of quark mass
1328 and field in the regularization invariant and schemes at three and four loops,”
1329 *Nuclear Physics B*, vol. 583, no. 1-2, pp. 3–34, Sep. 2000. DOI: 10.1016/s0550-
1330 3213(00)00331-x. [Online]. Available: <https://doi.org/10.1016%2Fs0550-3213%2800%2900331-x> (cit. on p. 12).
- 1332 [51] S. Weinberg, “New Approach to the Renormalization Group,” *Phys. Rev. D*,
1333 vol. 8, no. 10, pp. 3497–3509, Nov. 1973. DOI: 10.1103/PhysRevD.8.3497
1334 (cit. on p. 12).
- 1335 [52] R. L. Workman *et al.*, “Review of Particle Physics,” *PTEP*, vol. 2022, p. 083C01,
1336 2022. DOI: 10.1093/ptep/ptac097 (cit. on pp. 12, 14, 16, 20).
- 1337 [53] C. G. Callan, R. F. Dashen, and D. J. Gross, “The structure of the gauge
1338 theory vacuum,” *Physics Letters B*, vol. 63, no. 3, pp. 334–340, Aug. 1976.
1339 DOI: 10.1016/0370-2693(76)90277-X (cit. on p. 12).
- 1340 [54] J. L. Rosner, “CP symmetry violation,” Sep. 2001. arXiv: hep-ph/0109240
1341 (cit. on p. 12).
- 1342 [55] R. D. Peccei, “The Strong CP problem and axions,” *Lect. Notes Phys.*, vol. 741,
1343 M. Kuster, G. Raffelt, and B. Beltran, Eds., pp. 3–17, 2008. DOI: 10.1007/
1344 978-3-540-73518-2_1. arXiv: hep-ph/0607268 (cit. on p. 12).
- 1345 [56] J. J. Lodder, “On gluon masses, color symmetry, and a possible massive ninth
1346 gluon,” Jun. 1996. arXiv: hep-ph/9606317 (cit. on p. 12).
- 1347 [57] ”. Griffiths”, *Introduction to Elementary Particles*, ”2nd”. ”Wiley-VCH”,
1348 ”2008”, pp. 280–281, ISBN: ”978-3-527-40601-2” (cit. on p. 12).

- 1349 [58] T. Luthe, A. Maier, P. Marquard, and Y. Schroder, “Complete renormalization
 1350 of QCD at five loops,” *JHEP*, vol. 03, p. 020, 2017. DOI: 10.1007/
 1351 JHEP03(2017)020. arXiv: 1701.07068 [hep-ph] (cit. on p. 13).
- 1352 [59] B. Andersson, G. Gustafson, G. Ingelman, and T. Sjöstrand, “Parton fragmentation and string dynamics,” *Phys. Rep.*, vol. 97, no. 2-3, pp. 31–145,
 1353 Jul. 1983. DOI: 10.1016/0370-1573(83)90080-7 (cit. on pp. 13, 44).
- 1355 [60] ”. Wilson and others”, ”superconducting accelerator research and development at slac”, ”*SLAC-PUB*”, vol. ”749”, ”1970” (cit. on p. 14).
- 1357 [61] J. R. Finger and J. E. Mandula, “Quark pair condensation and chiral symmetry breaking in QCD,” *Nuclear Physics B*, vol. 199, no. 1, pp. 168–188, 1982,
 1358 ISSN: 0550-3213. DOI: [https://doi.org/10.1016/0550-3213\(82\)90570-3](https://doi.org/10.1016/0550-3213(82)90570-3).
 1359 [Online]. Available: <https://www.sciencedirect.com/science/article/pii/0550321382905703> (cit. on p. 15).
- 1362 [62] R. K. Ellis, W. J. Stirling, and B. R. Webber, *QCD and Collider Physics*
 1363 (Cambridge Monographs on Particle Physics, Nuclear Physics and Cosmology). Cambridge University Press, 1996. DOI: 10.1017/CBO9780511628788
 1364 (cit. on p. 17).
- 1366 [63] U. W. Heinz, “The Strongly coupled quark-gluon plasma created at RHIC,”
 1367 *J. Phys. A*, vol. 42, D. Neilson and G. Senatore, Eds., p. 214003, 2009. DOI:
 1368 10.1088/1751-8113/42/21/214003. arXiv: 0810.5529 [nucl-th] (cit. on
 1369 p. 18).
- 1370 [64] J. Letessier and J. Rafelski, *Hadrons and Quark-Gluon Plasma*. Oxford Uni-
 1371 versity Press, 2002, ISBN: 978-1-00-929075-3, 978-0-511-53499-7, 978-1-00-929070-
 1372 8, 978-1-00-929073-9. DOI: 10.1017/9781009290753 (cit. on p. 18).
- 1373 [65] A. Maire, “Phase diagram of QCD matter : Quark-Gluon Plasma,” General
 1374 Photo, 2015. [Online]. Available: <https://cds.cern.ch/record/2025215>
 1375 (cit. on p. 18).
- 1376 [66] J. Rafelski, “Connecting QGP-Heavy Ion Physics to the Early Universe,”
 1377 *Nucl. Phys. B Proc. Suppl.*, vol. 243-244, R. Battiston and S. Bertolucci, Eds.,
 1378 pp. 155–162, 2013. DOI: 10.1016/j.nuclphysbps.2013.09.017. arXiv:
 1379 1306.2471 [astro-ph.CO] (cit. on p. 19).

- 1380 [67] E. Annala *et al.*, “Evidence for quark-matter cores in massive neutron stars,”
1381 *Nature Phys.*, vol. 16, no. 9, pp. 907–910, 2020. DOI: 10.1038/s41567-020-
1382 0914-9. arXiv: 1903.09121 [astro-ph.HE] (cit. on p. 19).
- 1383 [68] F.-M. Liu and S.-X. Liu, “Quark-gluon plasma formation time and direct
1384 photons from heavy ion collisions,” *Phys. Rev. C*, vol. 89, no. 3, p. 034906,
1385 2014. DOI: 10.1103/PhysRevC.89.034906. arXiv: 1212.6587 [nucl-th]
1386 (cit. on p. 27).
- 1387 [69] Aug. 2021. [Online]. Available: <https://cerncourier.com/a/participants-and-spectators-at-the-heavy-ion-fireball/> (cit. on p. 29).
- 1389 [70] B. Abelev *et al.*, “Centrality determination of Pb-Pb collisions at $\sqrt{s_{NN}} =$
1390 2.76 TeV with ALICE,” *Phys. Rev. C*, vol. 88, no. 4, p. 044909, 2013. DOI:
1391 10.1103/PhysRevC.88.044909. arXiv: 1301.4361 [nucl-ex] (cit. on pp. 29,
1392 30).
- 1393 [71] “Centrality determination in heavy ion collisions,” Aug. 2018 (cit. on p. 30).
- 1394 [72] M. L. Miller, K. Reygers, S. J. Sanders, and P. Steinberg, “Glauber modeling
1395 in high energy nuclear collisions,” *Ann. Rev. Nucl. Part. Sci.*, vol. 57, pp. 205–
1396 243, 2007. DOI: 10.1146/annurev.nucl.57.090506.123020. arXiv: nucl-
1397 ex/0701025 (cit. on p. 30).
- 1398 [73] D. J. Gross and F. Wilczek, “Ultraviolet Behavior of Non-Abelian Gauge The-
1399 ories,” *Phys. Rev. Lett.*, vol. 30, no. 26, pp. 1343–1346, Jun. 1973. DOI:
1400 10.1103/PhysRevLett.30.1343 (cit. on p. 31).
- 1401 [74] H. Stoecker, “Collective flow signals the quark gluon plasma,” *Nucl. Phys. A*,
1402 vol. 750, D. Rischke and G. Levin, Eds., pp. 121–147, 2005. DOI: 10.1016/j.
1403 nuclphysa.2004.12.074. arXiv: nucl-th/0406018 (cit. on p. 31).
- 1404 [75] S. Cao and X.-N. Wang, “Jet quenching and medium response in high-energy
1405 heavy-ion collisions: a review,” *Rept. Prog. Phys.*, vol. 84, no. 2, p. 024301,
1406 2021. DOI: 10.1088/1361-6633/abc22b. arXiv: 2002.04028 [hep-ph] (cit.
1407 on p. 32).
- 1408 [76] A. Collaboration, “ATLAS Feature: Looking inside trillion degree matter,”
1409 General Photo, 2022. [Online]. Available: <https://cds.cern.ch/record/2809432> (cit. on p. 32).

- 1411 [77] C. Adler *et al.*, “Disappearance of back-to-back high p_T hadron correlations
 1412 in central Au+Au collisions at $\sqrt{s_{NN}} = 200\text{-GeV}$,” *Phys. Rev. Lett.*, vol. 90,
 1413 p. 082302, 2003. DOI: 10.1103/PhysRevLett.90.082302. arXiv: nucl-ex/0210033 (cit. on p. 33).
- 1415 [78] K. Aamodt *et al.*, “Elliptic flow of charged particles in Pb-Pb collisions at 2.76
 1416 TeV,” *Phys. Rev. Lett.*, vol. 105, p. 252302, 2010. DOI: 10.1103/PhysRevLett.
 1417 105.252302. arXiv: 1011.3914 [nucl-ex] (cit. on p. 34).
- 1418 [79] P. Bo źek, “Splitting of proton-antiproton directed flow in relativistic heavy-
 1419 ion collisions,” *Phys. Rev. C*, vol. 106, p. L061901, 6 Dec. 2022. DOI: 10.1103/
 1420 PhysRevC.106.L061901. [Online]. Available: <https://link.aps.org/doi/10.1103/PhysRevC.106.L061901> (cit. on p. 34).
- 1422 [80] M. Luzum and J.-Y. Ollitrault, “Directed flow at midrapidity in heavy-ion col-
 1423 lisions,” *Phys. Rev. Lett.*, vol. 106, p. 102301, 2011. DOI: 10.1103/PhysRevLett.
 1424 106.102301. arXiv: 1011.6361 [nucl-ex] (cit. on p. 34).
- 1425 [81] A. M. Poskanzer and S. A. Voloshin, “Methods for analyzing anisotropic flow
 1426 in relativistic nuclear collisions,” *Phys. Rev. C*, vol. 58, pp. 1671–1678, 3 Sep.
 1427 1998. DOI: 10.1103/PhysRevC.58.1671. [Online]. Available: <https://link.aps.org/doi/10.1103/PhysRevC.58.1671> (cit. on p. 35).
- 1429 [82] J. Cleymans *et al.*, “Statistical model predictions for particle ratios at $s(\text{NN})^{**}(1/2)$
 1430 $= 5.5\text{-TeV}$,” *Phys. Rev. C*, vol. 74, p. 034903, 2006. DOI: 10.1103/PhysRevC.
 1431 74.034903. arXiv: hep-ph/0604237 (cit. on p. 35).
- 1432 [83] A. Andronic, P. Braun-Munzinger, and J. Stachel, “Thermal hadron produc-
 1433 tion in relativistic nuclear collisions,” *Acta Phys. Polon. B*, vol. 40, pp. 1005–
 1434 1012, 2009. arXiv: 0901.2909 [nucl-th] (cit. on p. 35).
- 1435 [84] R. Hagedorn and J. Ranft, “Statistical thermodynamics of strong interactions
 1436 at high-energies. 2. Momentum spectra of particles produced in pp-collisions,”
 1437 *Nuovo Cim. Suppl.*, vol. 6, pp. 169–354, 1968 (cit. on p. 36).
- 1438 [85] F. Becattini and U. W. Heinz, “Thermal hadron production in p p and p anti-
 1439 p collisions,” *Z. Phys. C*, vol. 76, pp. 269–286, 1997, [Erratum: Z.Phys.C 76,
 1440 578 (1997)]. DOI: 10.1007/s002880050551. arXiv: hep-ph/9702274 (cit. on
 1441 p. 36).

- 1442 [86] J. Adam *et al.*, “Enhanced production of multi-strange hadrons in high-multiplicity
1443 proton-proton collisions,” *Nature Phys.*, vol. 13, pp. 535–539, 2017. DOI: 10.
1444 1038/nphys4111. arXiv: 1606.07424 [nucl-ex] (cit. on p. 37).
- 1445 [87] F. Becattini and J. Manninen, “Strangeness production from SPS to LHC,” *J.
1446 Phys. G*, vol. 35, J.-e. Alam *et al.*, Eds., p. 104013, 2008. DOI: 10.1088/0954-
1447 3899/35/10/104013. arXiv: 0805.0098 [nucl-th] (cit. on p. 36).
- 1448 [88] T. Pierog and K. Werner, “EPOS Model and Ultra High Energy Cosmic Rays,”
1449 *Nucl. Phys. B Proc. Suppl.*, vol. 196, J.-N. Capdevielle, R. Engel, and B.
1450 Pattison, Eds., pp. 102–105, 2009. DOI: 10.1016/j.nuclphysbps.2009.09.
1451 017. arXiv: 0905.1198 [hep-ph] (cit. on p. 37).
- 1452 [89] C. Bierlich *et al.*, “A comprehensive guide to the physics and usage of PYTHIA
1453 8.3,” Mar. 2022. DOI: 10.21468/SciPostPhysCodeb.8. arXiv: 2203.11601
1454 [hep-ph] (cit. on p. 37).
- 1455 [90] S. Roesler, R. Engel, and J. Ranft, “The Monte Carlo event generator DPMJET-
1456 III,” in *International Conference on Advanced Monte Carlo for Radiation
1457 Physics, Particle Transport Simulation and Applications (MC 2000)*, Dec.
1458 2000, pp. 1033–1038. DOI: 10.1007/978-3-642-18211-2_166. arXiv: hep-
1459 ph/0012252 (cit. on p. 37).
- 1460 [91] W. Cassing and E. L. Bratkovskaya, “Parton transport and hadronization from
1461 the dynamical quasiparticle point of view,” *Phys. Rev. C*, vol. 78, p. 034919,
1462 2008. DOI: 10.1103/PhysRevC.78.034919. arXiv: 0808.0022 [hep-ph] (cit.
1463 on pp. 37, 41).
- 1464 [92] W. Cassing and E. L. Bratkovskaya, “Parton-Hadron-String Dynamics: an
1465 off-shell transport approach for relativistic energies,” *Nucl. Phys. A*, vol. 831,
1466 pp. 215–242, 2009. DOI: 10.1016/j.nuclphysa.2009.09.007. arXiv: 0907.
1467 5331 [nucl-th] (cit. on pp. 37, 39).
- 1468 [93] W. Cassing, “From Kadanoff-Baym dynamics to off-shell parton transport,”
1469 *Eur. Phys. J. ST*, vol. 168, R. Alkofer, H. Gies, and B.-J. Schaefer, Eds., pp. 3–
1470 87, 2009. DOI: 10.1140/epjst/e2009-00959-x. arXiv: 0808.0715 [nucl-th]
1471 (cit. on p. 38).

- 1472 [94] O. Soloveva, J. Aichelin, and E. Bratkovskaya, “Transport properties and
1473 equation-of-state of hot and dense QGP matter near the critical endpoint in
1474 the phenomenological dynamical quasiparticle model,” *Phys. Rev. D*, vol. 105,
1475 no. 5, p. 054011, 2022. DOI: 10.1103/PhysRevD.105.054011. arXiv: 2108.
1476 08561 [hep-ph] (cit. on p. 39).
- 1477 [95] T. Sjostrand, “PYTHIA 5.7 and JETSET 7.4: Physics and manual,” Feb. 1994.
1478 arXiv: hep-ph/9508391 (cit. on p. 41).
- 1479 [96] W. Ehehalt and W. Cassing, “Relativistic transport approach for nucleus nu-
1480 cleus collisions from SIS to SPS energies,” *Nucl. Phys. A*, vol. 602, pp. 449–
1481 486, 1996. DOI: 10.1016/0375-9474(96)00097-8 (cit. on p. 42).
- 1482 [97] Y. Nambu and G. Jona-Lasinio, “Dynamical Model of Elementary Particles
1483 Based on an Analogy with Superconductivity. I,” *Physical Review*, vol. 122,
1484 no. 1, pp. 345–358, Apr. 1961. DOI: 10.1103/PhysRev.122.345 (cit. on p. 42).
- 1485 [98] T. Pierog *et al.*, “Epos lhc: Test of collective hadronization with data measured
1486 at the cern large hadron collider,” *Phys. Rev. C*, vol. 92, p. 034906, 3 Sep.
1487 2015. DOI: 10.1103/PhysRevC.92.034906. [Online]. Available: <https://link.aps.org/doi/10.1103/PhysRevC.92.034906> (cit. on pp. 43, 44).
- 1489 [99] Z. Wolff and D. Molnar, “Self-consistent Cooper-Frye freeze-out of a viscous
1490 fluid to particles,” *J. Phys. Conf. Ser.*, vol. 535, p. 012020, 2014. DOI: 10.
1491 1088/1742-6596/535/1/012020. arXiv: 1407.6413 [nucl-th] (cit. on p. 44).
- 1492 [100] S. Roesler, R. Engel, and J. Ranft, “The monte carlo event generator DPMJET-
1493 III,” in *Advanced Monte Carlo for Radiation Physics, Particle Transport Sim-
1494 ulation and Applications*, Springer Berlin Heidelberg, 2001. arXiv: 0012252
1495 [hep-ph] (cit. on p. 44).
- 1496 [101] A. Capella, U. Sukhatme, C.-I. Tan, and J. Tran Thanh Van, “Dual par-
1497 ton model,” *Phys. Rept.*, vol. 236, pp. 225–329, 1994. DOI: 10.1016/0370-
1498 1573(94)90064-7 (cit. on p. 44).